

Generalized whole-body Patlak parametric imaging for enhanced quantification in clinical PET

Nicolas A Karakatsanis¹, Yun Zhou², Martin A Lodge²,
Michael E Casey³, Richard L Wahl^{2,4}, Habib Zaidi^{1,5,6}
and Arman Rahmim^{2,7}

¹ Division of Nuclear Medicine and Molecular Imaging, School of Medicine, University of Geneva, Geneva, CH-1211, Switzerland

² Division of Nuclear Medicine, Department of Radiology, Johns Hopkins University, Baltimore, MD 21287, USA

³ Siemens Molecular Imaging, Knoxville, TN 37932, USA

⁴ Mallinckrodt Institute of Radiology, Washington University School of Medicine, St Louis, MO 63110, USA

⁵ Geneva Neuroscience Centre, University of Geneva, Geneva, CH-1211, Switzerland

⁶ Department of Nuclear Medicine and Molecular Imaging, University of Groningen, University Medical Center Groningen, Groningen, 9700 RB, Netherlands

⁷ Department of Electrical and Computer Engineering, Johns Hopkins University, Baltimore, MD 21287, USA

E-mail: nikolaos.karakatsanis@unige.ch, habib.zaidi@hcuge.ch
and arahmim1@jhmi.edu

Received 22 May 2015, revised 30 July 2015

Accepted for publication 8 September 2015

Published 28 October 2015



CrossMark

Abstract

We recently developed a dynamic multi-bed PET data acquisition framework to translate the quantitative benefits of Patlak voxel-wise analysis to the domain of routine clinical whole-body (WB) imaging. The standard Patlak (sPatlak) linear graphical analysis assumes irreversible PET tracer uptake, ignoring the effect of FDG dephosphorylation, which has been suggested by a number of PET studies. In this work: (i) a non-linear generalized Patlak (gPatlak) model is utilized, including a net efflux rate constant k_{loss} , and (ii) a hybrid (s/g)Patlak (hPatlak) imaging technique is introduced to enhance contrast to noise ratios (CNRs) of uptake rate K_i images. Representative set of kinetic parameter values and the XCAT phantom were employed to generate realistic 4D simulation PET data, and the proposed methods were additionally evaluated on 11 WB dynamic PET patient studies. Quantitative analysis on the simulated K_i images over 2 groups of regions-of-interest (ROIs), with low (ROI A) or high (ROI B) true k_{loss} relative to K_i , suggested superior accuracy

for gPatlak. Bias of sPatlak was found to be 16–18% and 20–40% poorer than gPatlak for ROIs A and B, respectively. By contrast, gPatlak exhibited, on average, 10% higher noise than sPatlak. Meanwhile, the bias and noise levels for hPatlak always ranged between the other two methods. In general, hPatlak was seen to outperform all methods in terms of target-to-background ratio (TBR) and CNR for all ROIs. Validation on patient datasets demonstrated clinical feasibility for all Patlak methods, while TBR and CNR evaluations confirmed our simulation findings, and suggested presence of non-negligible k_{loss} reversibility in clinical data. As such, we recommend gPatlak for highly quantitative imaging tasks, while, for tasks emphasizing lesion detectability (e.g. TBR, CNR) over quantification, or for high levels of noise, hPatlak is instead preferred. Finally, gPatlak and hPatlak CNR was systematically higher compared to routine SUV values.

Keywords: Patlak, whole-body, generalized, PET, quantification, detectability, parametric

(Some figures may appear in colour only in the online journal)

1. Introduction

Dynamic PET imaging allows for acquisition of valuable spatiotemporal activity concentration measurements to enable *in vivo* tracking of the physiological time course of the radiotracer. The obtained information, when utilized by tracer kinetic modeling methods, can then enable parametric PET imaging, a complementary framework of enhanced quantification (Carson 2005, Bentourkia and Zaidi 2006, 2007). The quantitative benefits of dynamic PET have motivated an increasing number of research studies covering a wide spectrum of medical imaging applications including in oncology (Hawkins *et al* 1992a, 1992b, Messa *et al* 1992, Fischman and Alpert *et al* 1993, Eary and Mankoff 1998, Gupta *et al* 1998, Delbeke 1999, Dimitrakopoulou-Strauss *et al* 2003, Prytz *et al* 2006).

Nevertheless, dynamic PET acquisitions have been primarily constrained to single-bed axial field-of-views (FOVs), due to preference for continuous temporal sampling of the FOV (Torizuka *et al* 1995, 2000). Thus, dynamic PET has been mainly associated with oncology studies, involving specific tumor types, as well as cardiac or neurological PET studies, where single-bed acquisitions are adequate (Jagust *et al* 1991, Lortie *et al* 2007). As a result, dynamic PET has not yet been translated into clinical routine, where whole-body (WB) acquisitions are important. In particular, oncology would appreciate the enhanced quantification across WB FOVs, as the likelihood for metastases from the primary tumor location to other regions dictates multi-bed diagnostic evaluations (Wahl and Buchanan 2002).

On the other hand, single-frame (i.e. static) WB PET imaging, relying on the standardized uptake value (SUV) metric, has been established in routine clinical practice, mainly because of the simplicity of WB PET scan protocols, its sufficient test-retest repeatability and extensively validated clinical utility (Kubota *et al* 1985, Wahl and Buchanan 2002, Thie 2004). At the same time, SUV can be considered as a semi-quantitative metric, since it does not account for tracer concentration in blood (input function) and largely depends on the post-injection scan time and the current metabolic status of each patient (Keyes 1995, Huang 2000, Paquet *et al* 2004, Thie 2004, Durand and Besson 2015). As a result, SUV PET evaluations and treatment response assessments may suffer from poor accuracy (Hoekstra *et al* 2000, 2002, Adams *et al* 2010, Boellaard 2011, de Langen *et al* 2012). A number of studies have

attempted to partially overcome these limitations by employing either (i) delayed or dual-time point WB SUV PET imaging (Hustinx *et al* 1999, Nakamoto *et al* 2000, Kubota *et al* 2001, Zhuang *et al* 2001, Matthies *et al* 2002, Nishiyama *et al* 2006), (ii) various normalization factors for SUV, such as patient weight, lean body mass and body surface area (Zasadny and Wahl 1993, Kim *et al* 1994) or (iii) simplified kinetic analysis (SKA) methods over regions-of-interest (ROIs) (Hunter *et al* 1996, Sadato *et al* 1998, Graham *et al* 2000, Freedman *et al* 2003, Sundaram *et al* 2004). Nevertheless, all methods above heavily rely on very specific assumptions to retain simplicity for clinical protocols. Examples include assumption of the time integral of input function as being proportional to injected dose divided by lean body mass, or that the proportion of non-phosphorylated to phosphorylated FDG is minimal at time of imaging, which may not be valid, compromising the accuracy of these methods (Freedman *et al* 2003, Sundaram *et al* 2004).

Recently, we proposed a PET acquisition and imaging framework enabling clinically feasible WB dynamic PET imaging, thus combining the benefits of multi-bed FOVs with the ability to obtain images of Patlak kinetic macro-parameters (Karakatsanis *et al* 2013a, 2013c). Quantitative analysis demonstrated enhanced tumor detectability over SUV in regions exhibiting high background signal, such as the liver. In this framework, the standard Patlak (sPatlak) linear graphical analysis had been selected as a robust modeling approach to directly estimate, from the reconstructed dynamic WB PET images, the tracer influx or uptake rate constant K_i and blood distribution volume V (Patlak *et al* 1983).

The sPatlak graphical analysis method arrives at a linear model equation only when an *irreversible* 2-tissue compartment tracer kinetic model is assumed, a common model for fluorodeoxyglucose (FDG) tracer in human organs and tumors (Phelps *et al* 1979, Patlak *et al* 1983, Kelloff *et al* 2005). However, a number of studies have reported clinical kinetic parameter values suggesting a non-negligible degree of apparent FDG uptake reversibility, or dephosphorylation, for many normal organs such as the liver, brain and lung as well as for tumors (Anchors *et al* 1977, Gallagher *et al* 1978, Phelps *et al* 1979, Huang *et al* 1980, Messa *et al* 1992, Okazumi *et al* 1992, 2009, Torizuka *et al* 1995, 2000, Nelson *et al* 1996, Delbeke 1999, Zhuang *et al* 2001, Dimitrakopoulou-Strauss *et al* 2006, Prytz *et al* 2006). As the sPatlak model inherently assumes irreversibility, it is forced to underestimate K_i in regions where a non-negligible underlying reversibility truly exists, to explain the progressive loss of the signal portion originating from the erroneously assumed 'irreversible' compartment (Patlak *et al* 1983, Patlak and Blasberg 1985). Consequently, when reversibility is neglected from model assumptions, the quantitative accuracy of K_i images may be compromised in certain regions, with negative implications for highly quantitative imaging tasks, such as treatment response monitoring for prognostic or theranostic purposes.

On the other hand, a *reversible* 2-tissue compartment kinetic model can properly account for underlying tracer dephosphorylation. Thus, an extended version of the sPatlak model, accepting the possibility of relatively small uptake reversibility, could enhance its accuracy by attributing the observed progressive signal intensity loss to an additional kinetic parameter rate constant: the tracer efflux rate constant. In fact, the theoretically expected K_i underestimation, when an irreversible compartment replaces a reversible one, has been also confirmed by a number of clinical dynamic PET studies, thus further suggesting the possibility for underlying FDG uptake reversibility in certain normal organs and tumors (Lammertsma *et al* 1987, Messa *et al* 1992, Choi *et al* 1994, Hasselbalch *et al* 2001, Graham *et al* 2002, Wu *et al* 2003, Hoh *et al* 2011, Sayre *et al* 2011).

Furthermore, although reversible FDG uptake kinetics are not as common for tumors as for normal tissues (Fischman and Alpert 1993, Messa *et al* 1992, Hawkins *et al* 1992b, Okazumi *et al* 1992, Nelson *et al* 1996, Graham *et al* 2000, Huang 2000, Zhuang *et al* 2001,

Lin *et al* 2005, Prytz *et al* 2006), certain tumor types with non-negligible reversibility have been reported, such as in the case of hepatocellular carcinomas (HCC) tumors (Messa *et al* 1992, Torizuka *et al* 1995). As a result, K_i estimates may be under- or even over-estimated and in various degrees at the target and background regions, depending on the presence (or not) of reversible kinetics in each region, thus affecting not only image quantification but also tumor-to-background contrast, potentially compromising tumor detectability as well. Moreover, as many normal tissues across the body reportedly exhibit some degree of reversibility, the likelihood of erroneous K_i quantification within PET FOV becomes higher with multi-bed acquisitions. Consequently, the need to include reversibility in the kinetic model analysis becomes even more evident in WB PET parametric imaging applications.

Therefore, in this study, we propose a novel generalized Patlak (gPatlak) multi-bed framework to enhance quantitative WB PET imaging including in regions exhibiting non-negligible uptake reversibility. We focus on oncology applications when the imaging task involves tumor detection and staging or treatment response assessments, but our findings could also apply to other tasks, such as quantitative PET-based differentiation of malignant versus benign tumors and WB imaging of inflammation, infection, etc. (Hübner *et al* 1996, Dimitrakopoulou-Strauss *et al* 2002, Basu and Alavi 2007, Sanz and Fayad 2008, Choi *et al* 2013, Oo *et al* 2013). In addition, we currently evaluate our proposed method for ^{18}F -FDG, the most common PET oncological radiotracer with well-modeled kinetics for a range of normal tissues and tumor regions across the human body (Phelps *et al* 1979, Hustinx *et al* 2002), though this approach could also apply to different radiotracers as well, such as ^{18}F -FLT (Been *et al* 2004), ^{18}F -FMISO (Thorwarth *et al* 2005), ^{18}F -Fluoride (Grant *et al* 2008, Siddique *et al* 2011, 2012, 2014), ^{18}F -Choline (Husarik *et al* 2008) and others (Groves *et al* 2007).

The extended Patlak method, originally proposed as theory and for region-based analysis by Patlak and Blasberg (1985), is equipped with an additional net efflux rate constant, k_{loss} , to properly account for tracer net uptake reversibility from the trapping or metabolic tissue compartment to the blood plasma. In fact, this model has been previously used in few PET studies involving FDG (Lodge *et al* 1999), ^{18}F -Fluorodopa brain (Holden *et al* 1997, Doudet *et al* 1998, Sossi *et al* 2001) as well as ^{18}F -Fluoride bone imaging (Siddique *et al* 2014) but only for ROI-based analysis and limited to a single bed.

In the present study, for the first time to our knowledge, an extended gPatlak method is implemented and assessed: (1) in the context of parametric imaging, i.e. involving kinetic parameters estimation at the voxel level, and (2) for WB dynamic acquisitions. The presented framework, also includes application of the basis function method (BFM) to effectively linearize the parameter estimation process in a computationally efficient algorithm (Gunn *et al* 1997). In addition, a hybrid parametric imaging method (hPatlak) is proposed which selectively applies either standard or generalized Patlak method at each voxel, according to a Patlak correlation-based binary classification scheme, to enhance tumor contrast-to-noise ratio (CNR) and detectability in K_i images at the cost of quantification compared to gPatlak.

2. Materials and methods

2.1. Generalized Patlak graphical analysis

The linear Patlak model utilizes dynamic PET image data and the time course of blood plasma tracer concentration (input function) to estimate through linear regression the kinetic macro-parameters of tracer net influx rate constant K_i and the total blood distribution volume V at each voxel employing the following model equation (Patlak *et al* 1983):



Figure 1. (left) Two-tissue compartment kinetic models (a) without and (c) with reversibility for FDG tracer.

$$\frac{C(t_n)}{C_P(t_n)} = K_i \frac{\int_0^{t_n} C_P(\tau) d\tau}{C_P(t_n)} + V, \quad t_n > t^*, \quad n = 1 \dots N \tag{1}$$

where $C(t)$ is the measured time activity curve (TAC) at each voxel, $C_P(t)$ is the blood plasma TAC or input function estimated either from an image ROI or from blood sampling, t_n with $n = 1 \dots N$ denote the mid-time points for the N dynamic PET frames/measurements and t^* is the time after which relative kinetic equilibrium between the blood and the reversible compartment is attained. The standard Patlak equation describes the linear relationship between (i) the ratio of the measured tissue $C(t)$ to the plasma $C_P(t)$ activity concentration and (ii) the ratio of the running time integral of the plasma TAC to the plasma TAC, the latter also denoted as ‘normalized’ or ‘stretched’ time (Holden *et al* 1997).

Later, Patlak and Blasberg (1985) introduced an extended and more general graphical analysis model to account for potential reversible uptake rate. Thus, an additional kinetic parameter was introduced, here denoted as k_{loss} , to describe the net rate constant for metabolized tracer loss to the blood plasma (net efflux rate constant). By assuming $k_{loss} \ll K_i$ the following non-linear Patlak equation can be obtained for the kinetic analysis of m dynamic frames:

$$\frac{C(t_n)}{C_P(t_n)} = K_i \frac{\int_0^{t_n} e^{-k_{loss}(t_n-\tau)} C_P(\tau) d\tau}{C_P(t_n)} + V, \quad t_n > t^*, \quad n = 1 \dots N \tag{2}$$

where $K_i = K_1 k_3 / (k_2 + k_3)$ and $k_{loss} = k_2 k_4 / (k_2 + k_3)$ as defined by Patlak and Blasberg (1985).

As the newly introduced k_{loss} parameter is included in an exponential term, the kinetic parameter estimation problem now becomes non-linear. As it will be demonstrated later, the accuracy of the two Patlak models depends on the ratio of k_{loss}/K_i . Sossi *et al* (2001) in particular also studied, in the case of region-based ^{18}F -fluorodopa brain PET tracer kinetic analysis for Parkinson’s disease evaluations, the effect of this ratio, which they term as ‘effective dopamine turnover’ (EDT).

The standard Patlak model assumes a 2-tissue compartment model involving 3 parameter rate constants (K_1 , k_2 and k_3) with the second compartment considered irreversible, i.e. $k_4 = 0$ (figure 1(a)). The measured tracer tissue concentration $C(t)$ is defined as the sum of the extravascular $C_e(t)$ and the metabolized $C_m(t)$ tracer tissue concentrations. By reformulating equation (1) that:

$$C(t_n) = K_i \int_0^{t_n} C_P(\tau) d\tau + VC_P(t_n) = K_i \otimes C_P(t_n) + VC_P(t_n), \quad t_n > t^*, \quad n = 1, \dots, N \tag{3}$$

where \otimes denotes the mathematical operation of single-dimensional (1D) convolution in the time domain.

On the other hand, the non-linear Patlak model assumes a two compartment kinetic model with a non-negative k_d rate constant (figure 1, bottom left). Similarly, by restructuring equation (2) we have:

$$\begin{aligned}
 C(t_n) &= K_i \int_0^{t_n} e^{-k_{\text{loss}}(t_n-\tau)} C_P(\tau) d\tau + VC_P(t_n) \\
 &= (K_i e^{-k_{\text{loss}} t_n}) \otimes C_P(t_n) + VC_P(t_n), \quad t_n > t^*, \quad n = 1, \dots, N.
 \end{aligned}
 \tag{4}$$

2.2. Whole-body non-linear parametric image estimation

In the case of the linear sPatlak model (equation (1) or (3)), the two parameters of interest, K_i and V , can be estimated directly using the ordinary least squares (OLS) linear regression method. Let us consider the following sPatlak regression model:

$$\mathbf{Y}^j = \mathbf{X}_s \boldsymbol{\beta}^j + \boldsymbol{\varepsilon}^j \tag{5a}$$

where:

$$\mathbf{Y}^j = \begin{bmatrix} C^j(t_1) & \dots & C^j(t_N) \end{bmatrix}^T, \quad \mathbf{X}_s = \begin{bmatrix} \int_0^{t_1} C_P(\tau) d\tau & C_P(t_1) \\ \vdots & \vdots \\ \int_0^{t_N} C_P(\tau) d\tau & C_P(t_N) \end{bmatrix}, \quad \boldsymbol{\beta}^j = \begin{bmatrix} K_i^j & V^j \end{bmatrix}^T.$$

Note in equation (5a) that the input function measurements in standard Patlak model matrix \mathbf{X}_s and the TACs column vector \mathbf{Y} are linearly related with the unknown sPatlak kinetic macro-parameters $\boldsymbol{\beta}$ (slope K_i and intercept V). This relationship can be expanded into the following set of sPatlak N bilinear equations:

$$C(t_n) = K_i \int_0^{t_n} C_P(\tau) d\tau + VC_P(t_n) + \varepsilon_n, \quad t_n > t^*, \quad n = 1, \dots, N. \tag{5b}$$

However, for the non-linear gPatlak model (equation (2) or (4)), we propose an efficient implementation of the basis function method (BFM) (Gunn *et al* 1997) as we have presented in a preliminary work (Karakatsanis *et al* 2013d). Initially, a pool of discrete candidate k_{loss} values has to be determined. The range $[10^{-5}, 10^{-1}]$ of $M = 10^4$ candidate k_{loss} values, in units of s^{-1} , is recommended, according to equation (7) and a wide collection of k -values, as reported in the literature (Okazumi *et al* 1992, 2009, Torizuka *et al* 1995, 2000, Dimitrakopoulou-Strauss *et al* 2006), a subset of which was later utilized to conduct simulations (table 1). Then a set of M basis functions, each representing one of the M candidate k_{loss} values, is constructed to effectively linearize the non-linear parameters estimation problem:

$$\omega_m(t_n) = C_P(t_n) \otimes e^{-k_{\text{loss}}^m t_n}, \quad m = 1 \dots M, \quad n = 1 \dots N. \tag{6}$$

After replacing the exponential term in equation (4) with each of the M basis functions (equation (6)), the following set of M bilinear Patlak equations is constructed:

$$\mathbf{Y}^j = \mathbf{X}_m^j \boldsymbol{\beta}_m^j + \boldsymbol{\varepsilon}_m^j, \quad m = 1 \dots M. \tag{7a}$$

The definitions of the generalized Patlak model matrix \mathbf{X}_m^j and the unknown kinetic macro-parameters vector $\boldsymbol{\beta}_m^j$ of Patlak slope $K_i^{j,m}$ and intercept $V^{j,m}$ depend, each time, on the currently selected m th basis function ω_m as follows:

Table 1. K rate parameters.

Regions	K_1	k_2	k_3	k_4	V_B
Normal liver	0.864	0.981	0.005	0.016	—
Liver tumor	0.243	0.78	0.1	0	—
Normal lung	0.108	0.735	0.016	0.013	0.017
Lung tumor	0.301	0.864	0.097	0.001	0.168
HCC tumor	0.283	0.371	0.057	0.012	—
Myocardium	0.6	1.2	0.1	0.001	—

$$\mathbf{X}_m^j = \begin{bmatrix} \int_0^{t_1} e^{-k_{\text{loss}}^{j,m}(t_1-\tau)} C_P(\tau) d\tau & C_P(t_1) \\ \vdots & \vdots \\ \int_0^{t_N} e^{-k_{\text{loss}}^{j,m}(t_N-\tau)} C_P(\tau) d\tau & C_P(t_N) \end{bmatrix}, \quad \beta_m^j = \begin{bmatrix} K_i^{j,m} & V^{j,m} \end{bmatrix}^T. \quad (7b)$$

Or, equivalently, we have M different sets of equations, where each set is composed of N bilinear Patlak formulas:

$$C(t_n) = K_i^{j,m} \omega_m(t_n) + V^{j,m} C_P(t_n) + \varepsilon_n, \quad t_n > t^*, \quad m = 1 \dots M, \quad n = 1, \dots, N. \quad (7c)$$

Thus the original non-linear parameter estimation problem (equation (4)) has now been translated to a set of n linear estimation problems (equation (7c)), as many as the initially selected number of basis functions or candidate k_{loss} values. Therefore, the standard linear OLS regression can then be applied to each of the n linearized Patlak equations in order to estimate the respective set of K_i^j and V^j parameters for the selected k_{loss}^j value. Subsequently, the corresponding residual sum of squared error RSS_j between our measurements \mathbf{Y} and our estimates $\hat{\mathbf{Y}}_j = \mathbf{X}\hat{\beta}_j$ is calculated:

$$\text{RSS}_{j,m} = (\mathbf{Y} - \mathbf{X}\hat{\beta}_m^j)^T (\mathbf{Y} - \mathbf{X}\hat{\beta}_m^j), \quad \hat{\beta}_j = \begin{bmatrix} K_i^j & V^j \end{bmatrix}^T. \quad (8)$$

The paired set of estimated parameters $\hat{\beta}_m^j$ and $k_{\text{loss}}^{j,m}$, for which the minimum $\text{RSS}_{j,m}$, for a fixed j th voxel over all M RSS scores, was observed, is finally selected as the final BFM parametric estimate:

$$\hat{\beta}_{\text{BFM}}^j = \{\hat{\beta}_{m_{\text{opt}}}^j, k_{\text{loss}}^{j,m_{\text{opt}}}\}, \quad m_{\text{opt}} = \arg \min_m \{\text{RSS}_{j,m}\},$$

$$\hat{\beta}_{m_{\text{opt}}}^j = \begin{bmatrix} K_i^{j,m_{\text{opt}}} & V^{j,m_{\text{opt}}} \end{bmatrix}^T. \quad (9)$$

By repeating the BFM estimation algorithm for each voxel, a set of K_i , k_{loss} and V parametric images can be produced in the end.

2.3. Hybrid generalized Patlak imaging

Multi-bed dynamic PET acquisition involves short frames (e.g. 45 s/bed in this study) non-continuously acquired over time at each bed position and with relatively large time gaps between the frames, thus tending to enhance noise levels compared to single-bed dynamic protocols. In addition, gPatlak method is non-linear involving three parameters as opposed to two for the linear sPatlak. As a result, noise may be considerable for gPatlak, though it is still expected to be lower than for full compartmental kinetic analysis (Carson *et al* 2005). For that

reason, although gPatlak might enhance K_i estimates at the tumor ROIs, the respective (tumor-to-background) contrast to (background) noise ratio (CNR) metric, an important detectability index, may not be similarly enhanced, due to noise elevation at the background.

Therefore, in this work we also propose a novel hybrid parametric imaging method, namely hybrid Patlak (hPatlak), involving the selective application of either sPatlak or gPatlak analysis at every voxel, aiming for higher K_i CNR scores than those achieved by gPatlak or sPatlak alone, by exploiting the expected higher tumor contrast of the former and the low background noise of the latter within the same analysis framework. Consequently, hPatlak is not expected to be as quantitative as gPatlak, although it is more accurate than sPatlak. Our main motivation with hPatlak is to provide a complimentary method that would improve tumor detectability by targeting enhancement of tumor CNR scores.

The selection of the applied Patlak method at each voxel is based on the quantitative criterion of weighted Patlak correlation-coefficient WR, an index of the degree of linear correlation between the dynamic PET measurements and the sPatlak assumptions. By considering the sPatlak analysis, equation (1) can be rewritten, for a given dynamic frame n , as follows:

$$y_n = K_i x_n + V, \quad y_n = \frac{C(t_n)}{C_P(t_n)}, \quad x_n = \frac{\int_0^{t_n} C_P(\tau) d\tau}{C_P(t_n)}, \quad n = 1 \dots N. \quad (10)$$

Then the weighted voxel-wise Patlak correlation coefficient WR can be calculated as follows [16]:

$$WR = \frac{\sum_n w_n \sum_n w_n x_n y_n - \sum_n w_n x_n \sum_n w_n y_n}{\sqrt{\left[\sum_n w_n \sum_n w_n x_n^2 - \left(\sum_n w_n x_n \right)^2 \right] \left[\sum_n w_n \sum_n w_n y_n^2 - \left(\sum_n w_n y_n \right)^2 \right]}}. \quad (11)$$

The weights are defined as a function of the time duration Δt_n and sinogram total counts c_n in frame n :

$$w_n = \frac{(\Delta t_n)^2}{c_n}, \quad \Delta t_n \stackrel{\text{def}}{=} t_n^{\text{end}} - t_n^{\text{start}}, \quad n = 1 \dots N.$$

After repeating the previous Patlak correlation calculations for every voxel TAC, a weighted Patlak correlation image (WR-image) can be generated from the acquired set of dynamic PET images.

The WR correlation metric essentially quantifies how well correlated each measured voxel TAC is with the sPatlak assumptions. In a hypothetical noise-free scenario, all measured voxel TACs would highly correlate with sPatlak model assumptions, regardless of the presence of uptake reversibility. Also, WR would approach unity in all voxel regions where underlying k_{loss} is nearly zero. However, in real dynamic PET scans, particularly when extended to the WB, noise can be considerably high, due to the short frames and the sparse temporal sampling at each bed. As the noise increases, WR is expected to drop in values. Thus, it is reasonable to expect that regions of lower uptake and, therefore, higher noise, such as most of the background normal tissue regions, will exhibit lower Patlak correlation coefficients, while regions of higher uptake and therefore better count statistics and lower noise, such as myocardium and most of suspected tumors, will be associated with relatively higher correlation coefficients. In fact, we have systematically observed that high Patlak correlation clusters are likely associated with voxel TACs of low noise, usually corresponding to tumors or high uptake regions, while low Patlak correlation cluster often

characterizes voxel TACs in regions of low uptake, such as in tumor background (Zasadny and Wahl 1996, Karakatsanis *et al* 2013a, 2013d). In addition, WR correlation may be also diminished for voxel TACs affected by bulk body motion across the different WB dynamic frames.

As a result, the proposed WR correlation-coefficient metric may act as an effective binary classification method between regions of low and high levels of noise or motion contamination. This feature can be utilized to selectively apply the less precise but more accurate non-linear BFM gPatlak parameter estimation method only to the highly correlated and statistically more reliable voxel TACs. By contrast, the more robust but potentially not as accurate sPatlak method can be selected for the remaining less correlated voxel TACs. An extra degree of freedom is introduced with the proposed hPatlak regression method thanks to the role of WR threshold, a free parameter quantitatively determining the level of Patlak correlation above which a voxel TAC can be characterized as of high correlation. Based on our clinical findings, we propose an initial *range* of possible WR threshold values between 0.75 and 0.98.

Initially, a user-defined correlation threshold is picked to classify the voxels of the WR-image into 2 clusters of relatively high (hWR cluster) and low (lWR cluster) Patlak correlation. Subsequently, gPatlak is assumed for the hWR voxel TACs, while sPatlak is used for the lWR voxel TACs. Non-linear BFM is employed for the estimation of the K_i , k_{loss} and V parameters in the hWR cluster, while OLS is applied for K_i and V parameter estimation in the lWR cluster. Thus, the k_{loss} parameter is assumed to be zero for the lWR voxels. In the end, a set of hybrid K_i , k_{loss} and V parametric images is created. A flow chart illustrating the principal steps of the proposed hybrid parametric imaging method is presented in figure 2.

Obviously, hPatlak images will depend on the selection of the WR threshold. Therefore, for the clinical routine application of hPatlak through an image analysis software, we suggest performing this method for a predetermined number of WR thresholds, within our recommended range of [0.75 0.98]. Then, a sliding bar interface can be provided to enable online inspection of the corresponding hPatlak images while sliding over the predetermined WR threshold values. Thus, users may instantly visualize the effect of WR threshold on the hPatlak K_i images over a range of correlation-coefficients and select the most appropriate threshold for the targeted imaging task. The extra computational cost of such type of analysis is negligible, as hPatlak images can be readily synthesized from the generated gPatlak and sPatlak images.

2.4. Simulation and clinical studies

2.4.1. Dynamic multi-bed acquisition. In both simulations and clinical studies, a previously validated dynamic multi-bed PET acquisition protocol was employed, after being optimized for clinically feasible acquisitions (Karakatsanis *et al* 2011) and according to the system specifications of current commercial clinical PET/CT scanners. The protocol consists of:

- (i) an initial single-bed dynamic scan over the heart to acquire the initial phase (first 6-min post-injection) of the input function, followed by
- (ii) a sequence of 6 WB passes, corresponding to a total time window of 10–45 min post-injection.

All bed positions were scanned in step-and-shoot mode for 45 s/bed to ensure enough counts per dynamic frame while allowing for a sufficient number of 6 passes in the clinically available time window (10–45 min post-injection) before the SUV static PET WB scan (figure 3).

In addition, two commercially available clinical PET/CT scanners were used for performance evaluation of the proposed method on clinical WB dynamic data. Initially, the GE Discovery RX scanner was utilized where the optimization of the acquisition protocol had been performed (Karakatsanis *et al* 2011), while later the more recent Siemens Biograph mCT scanner was employed to assess the performance of the proposed methods on a state-of-the-art

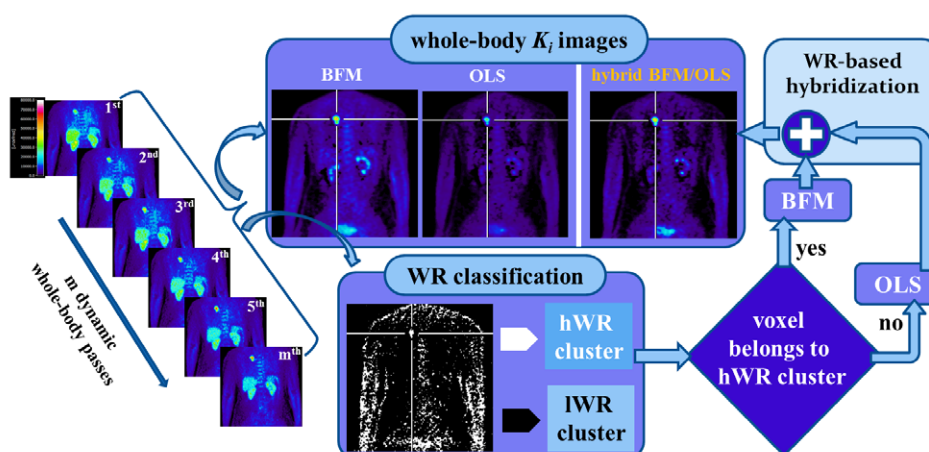


Figure 2. Flow chart illustrates the WR-based hPatlak imaging method. In the WR image, all voxels have been assigned either to the hWR (white) or IWR (black) cluster, according to their calculated WR coefficient value and a user-selected WR threshold (0.95 in this case). The depicted WR image classification may considerably change for different WR thresholds and patients but hWR cluster usually tends to include the high focal uptake regions.

clinical PET/CT scanner with time-of-flight (TOF) and point-spread-function (PSF) resolution modeling capabilities (Jakoby *et al* 2011). A preliminary evaluation study of the benefits of TOF and PSF features in WB parametric PET imaging are presented here (Karakatsanis *et al* 2014b). The same acquisition protocol was applied for both scanners, to ensure a common ground when comparing the results.

2.4.2. Generation of simulated data. An extensive literature review was conducted to collect a characteristic set of FDG k -values (table 1) (Okazumi *et al* 1992, 2009, Torizuka *et al* 1995, 2000, Dimitrakopoulou-Strauss *et al* 2006). The kinetic data were used together with a 2-compartment 4-parameter kinetic model (figure 1(c)) and the Feng input function model (Feng *et al* 1993) to generate realistic noise-free TACs (figure 4(a)), that were later assigned to the XCAT phantom (figure 4(b)). Then, lung and liver spherical tumors of 15 mm and 10 mm in diameter were placed within the normal XCAT organs of lung and liver respectively. Table 1 includes a wide range of k -micro parameter values corresponding to a k_{loss} range from zero or negligible up to very high values, i.e. comparable to K_i . We chose to evaluate such a wide range of FDG kinetics in order to validate the proposed gPatlak method under all potential clinical scenarios. We should also note that the very high k_4 and respective k_{loss} values were considerably less frequent in the literature.

The resulting dynamic XCAT bed frames were used as input to perform analytic 4D simulations, using STIR open-source package, with realistic levels of Poisson noise determined by the number of counts per frame, as calculated based on the reported sensitivity of the mCT scanner, the 3D acquisition properties (e.g. max. ring difference and span factor), the injected activity, the FDG tracer decay and the time duration of each frame (Thielemans *et al* 2012). A total of $n = 15$ Poisson noise realizations were produced. Subsequently, the generated 4D simulated data were reconstructed with the ML-EM iterative reconstruction algorithm as implemented within the OS-MAP-OSL application of STIR reconstruction suite (Thielemans

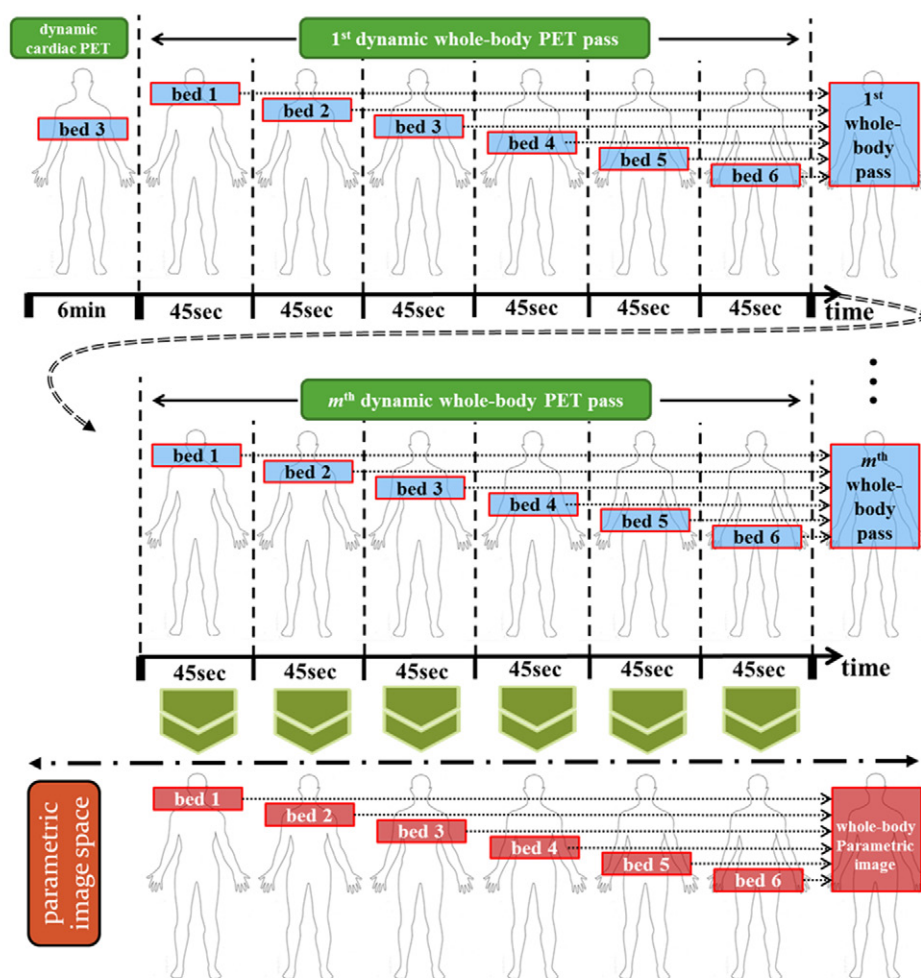


Figure 3. Flowchart of the two WB dynamic acquisition protocols involving an initial 6min single-bed dynamic scan over the heart to acquire the initial part of the input function followed by m dynamic WB passes scanned in the same direction (head-to-feet in this case), each consisting of 6 beds, each scanned for 45 s.

et al 2012). Finally the dynamic reconstructed PET images from various iteration steps and all noise realizations were analyzed according to sPatlak, gPatlak and hPatlak methods to produce respective WB K_i images. The generated images were then quantitatively analyzed in terms of noise versus bias, tumor-to-background (TBR) contrast and CNR performance at selected lung and liver tumor ROIs.

2.4.3. Clinical studies. In addition, the clinical performance of the proposed gPatlak and hPatlak WB K_i imaging methods was evaluated for a set of $n = 11$ WB patient dynamic PET studies, of which the first six were obtained on the GE Discovery RX PET/CT scanner while the last five were acquired on the state-of-the-art Siemens Biograph mCT TOF PET/CT scanner, both installed at the Johns Hopkins PET center. In all clinical cases, the optimized WB dynamic acquisition protocol of figure 3 has been applied. The utilization of two widely

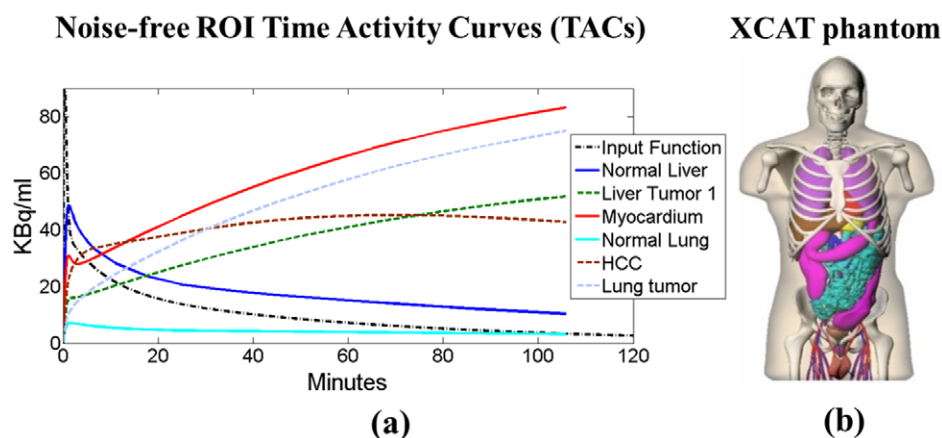


Figure 4. (a) Noise-free time activity curves for different regions, as generated using a 2 compartment kinetic model and the k -values of table 1. (b) The XCAT phantom where the TACs were assigned to produce the dynamic data.

applicable modern clinical PET/CT scanners and the acquisition of oncology patient data allowed us to validate the proposed methods under a broad range of acquisition conditions often present in PET imaging centers nowadays.

3. Results

3.1. Tracer kinetic simulation studies

Figure 5(a) shows, on the left, the true K_i image from a cardiac bed FOV, as constructed by directly assigning the true K_i values, calculated from the k -micro-parameters of table 1 and equation (6), to the respective ROIs of normal organs (including liver, lung and myocardium) and tumor types A and B of 15 mm (A1, B1) and 10 mm (A2, B2) diameter respectively.

The central and right images of figure 5(a) represent the estimated sPatlak and gPatlak K_i cardiac images, as derived by application of the respective Patlak model on 6 noise-free dynamic PET cardiac frames, acquired at exactly the time frames corresponding to our proposed WB dynamic PET scan protocol (figure 3). By visual comparison of sPatlak and gPatlak with respect to true K_i image, significant underestimation (bias) in the normal liver and tumor ROIs B1 and B2 is evident for sPatlak, while gPatlak nearly eliminates bias. As the data are noise-free, underestimation of K_i can be attributed to model-related factors and, in particular, the erroneous sPatlak assumption for zero k_{loss} while, in fact it had been simulated as positive for those two particular ROIs. On the contrary, gPatlak method is able to estimate K_i with a considerably smaller bias after accounting for the underlying presence of non-zero k_{loss} . Moreover, we plot in figure 5(b) the Feng input function model (Feng *et al* 1993) and the simulated noise-free FDG TACs for B2 tumor. The latter was produced after convolving the impulse response function of the 2-tissue compartment 4-parameters model (figure 1(c)) with the modeled input function (Carson *et al* 2005). Due to a non-negligible simulated k_{loss} value, with respect to K_i , B2 tumor TAC is reduced at later times.

Then, we present in figure 5(c) two groups of noise-free Patlak plots, as derived from simulated tumor B2 kinetics employing either sPatlak or gPatlak graphical analysis. The true k -values from table 1 are used as simulations input. For each method, the modeled (true) and ROI-based Patlak curves are plotted. The former is calculated from Patlak analysis on TACs

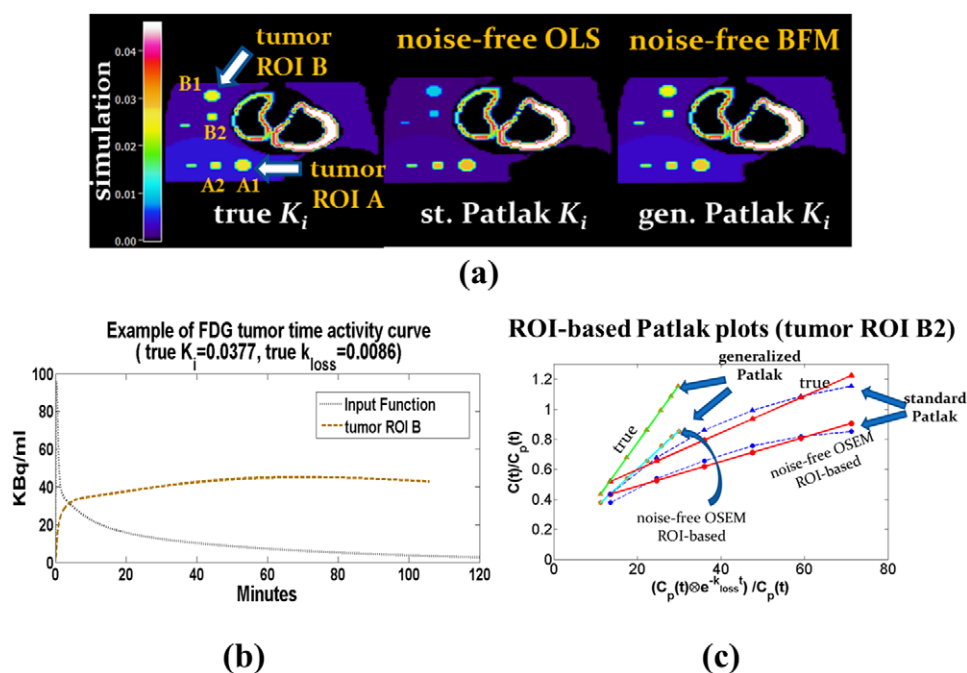


Figure 5. (a) Simulated Patlak K_i images of a cardiac XCAT bed, where 2 sets of spherical homogeneous tumor ROIs are identified: A1 (large), A2 (small) and B1 (large), B2 (small). Same underlying (true) kinetics were originally assigned between A1 and A2 ROIs (type A kinetics) and between B1 and B2 ROIs (type B kinetics) of the true PET frames. True K_i image was derived from direct assignment of true K_i values, while sPatlak and gPatlak noise-free K_i images were generated with sPatlak-OLS and gPatlak-BFM analysis, respectively, on 6 noise-free PET frames. (b) Noise-free simulated input function and tumor ROI B1 or B2 TACs (same kinetics assigned to B1 and B2), as generated using the 2 compartment model (figure 1(c)), demonstrating decrease of activity at later times, due to underlying k_{loss} reversibility. (c) Noise-free plots for sPatlak and gPatlak models after analyzing simulated tumor ROI B2 TAC, either directly modeled from k -values or extracted from B2 ROI on reconstructed dynamic PET images. The reduced slope of sPatlak and gPatlak plots for the B2 ROI extracted data, with respect to modeled B2 TAC case, is attributed to the partial volume error for the small B2 tumor.

directly modeled from the true k -values after convolving with the Feng input function model, while the latter is derived from ROI-based Patlak analysis on noise-free reconstructed images (ML-EM, 5 iterations), thus suffering from partial volume error (PVE) effect. All 4 Patlak curves are plotted in the same diagram, as gPatlak definition for stretched time variable in horizontal axis applies for sPatlak model too, assuming zero k_{loss} in that case. By comparing the true and ROI-based plots for each model, an underestimation of the curves slope (K_i) is observed for the latter, which is attributed to PVE, an effect inherent in the tomographic reconstruction process, particularly for smaller tumors (such as B2).

In addition, the modeled (true) data, when plotted in the Patlak diagram assuming zero k_{loss} , are not forming straight lines, as would have been expected by sPatlak, but instead exhibit a curvature (negative second derivative), resulting in OLS-fitted straight lines of reduced slope (first derivative), thus underestimating K_i . On the other hand, after accounting for true k_{loss} , the same data are aligned to form a nearly straight line. As a result, the OLS-fitted straight

line is then associated with a relatively increased slope or K_i . The same effect between the two models was also observed for the ROI-based analysis.

Since sPatlak plot assumes $k_{\text{loss}} = 0$ (equation (1)) while in fact simulation input involves positive k_{loss} (B2 tumor true $k_{\text{loss}} = 0.0086$), sPatlak is consequently overestimating the stretched time (horizontal axis variable) for a given ratio of tissue to plasma signal (vertical axis variable). On the other hand, gPatlak recovers the expected linear relationship in the Patlak plot by correcting for the loss of metabolized tracer after multiplying the stretched time with the term $\exp(-k_{\text{loss}}t)$ (equation (2)). In figure 5(c), the negative curvature of Patlak plot for standard model, as well as its linearization when gPatlak assumptions are utilized, provide intuitive graphical illustrations for the actual causes of sPatlak K_i underestimation and the correcting effect of gPatlak.

The % error (bias) quantitative analysis on the noise-free dynamic data for K_i and k_{loss} estimates is presented in figures 5 and 6, respectively. The plots suggest a considerable reduction of % bias for both parameters and for a large range of k_{loss}/K_i ratios when gPatlak replaces sPatlak method. However, our results also confirm the limitations of gPatlak accuracy when true k_{loss} becomes too high, i.e. comparable to K_i , as also expected from the theory (Patlak and Blasberg 1985). In particular, in figure 6(a), the % bias is equally zero for both models when underlying $k_{\text{loss}} = 0$, irrespective of k_3 or K_i , as expected from equations (1) and (3) too. However, as true k_{loss} increases (assuming only k_4 increases, with the rest of the parameters constant) sPatlak K_i % bias increases dramatically, while for gPatlak it does not exceed 5%, for small k_{loss} values. In addition, a further decrease of k_3 , such that $0 < k_{\text{loss}}/K_i < 2$, assuming K_1 and k_2 constant, causes an additional but relatively milder increase of K_i % bias which however never exceeds 10% for gPatlak. It should be noted that, based on our collection of FDG tracer k -values from literature, the range of k_{loss} and K_i is always such that $0 < k_{\text{loss}}/K_i < 1.5$ with ratio values higher than 1 rarely observed in real data. In this study, we initialized our investigation with a set of k -values from literature and then carefully expanded our search space to more extreme cases such that $0 < k_{\text{loss}}/K_i < 2$. This allowed us to validate gPatlak K_i bias in extreme cases, i.e. when k_{loss} is comparable to K_i , in the absence of noise.

The previous K_i % bias analysis for the same tumor region was repeated for a 30–90 min post-injection (p.i.) acquisition time window (figure 6(b)) confirming our conclusions above. However, the observed sPatlak K_i % bias for the 30–90 min protocol is relatively larger than for 0–45 min window. On the other hand, gPatlak K_i % bias is consistently low, irrespective of the acquisition time window, demonstrating the quantitative significance of gPatlak when (a) dynamic acquisitions last longer, as is inherently the case with WB dynamic protocols, or (b) they are delayed to include the time window of static SUV PET scans (60–80 min p.i.), as we recently proposed for combined SUV/Patlak imaging (Karakatsanis *et al* 2015).

A similar % bias analysis for noise-free simulated data was repeated for the k_{loss} parameter as well. Figure 7(a) shows a very good correlation between the estimated noise-free k_{loss} and the true k_{loss} value, as the latter increases, for a range of true k_{loss} values commonly found in the literature ($0 < k_{\text{loss}} < 0.04$). The % k_{loss} bias was evaluated with respect to k_{loss}/K_i ratio, assuming K_1 , k_2 and k_3 constant for each error plot and only decreasing k_3 between different plots. As figure 7(b) illustrates, k_{loss} % bias never exceeds 10% for $0 < k_{\text{loss}}/K_i < 1$. The same k -values search space as for K_i bias analysis has been used here too.

3.2. Realistic 4D tomographic simulations

The resulting K_i images from the sPatlak, gPatlak and hPatlak analysis of the reconstructed noisy simulated data are presented in figure 8(a) along with the quantitative noise versus bias analysis over 4 tumor ROIs: A1, A2, B1 and B2 in figures 8(b)–(e) respectively. For

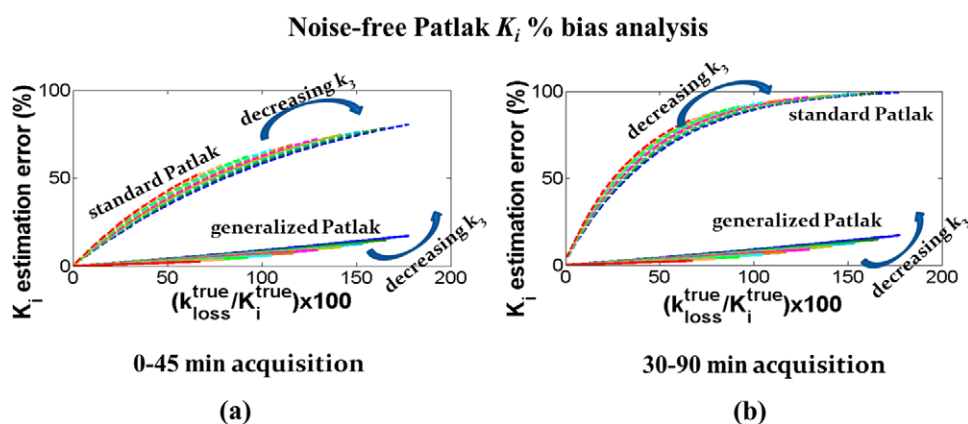


Figure 6. Noise-free K_i estimation error (% bias) curves versus true k_{loss}/K_i (by effectively increasing k_4 for each curve) for (b) 10–45 m and (c) 30–90 m acquisition protocol. The different color curves in both (a) and (b) correspond to a range of k_3 published values such that true $0 < k_{loss}/K_i < 2$. Also K_1 and k_2 are constant and correspond to the lung tumor case (table 1).

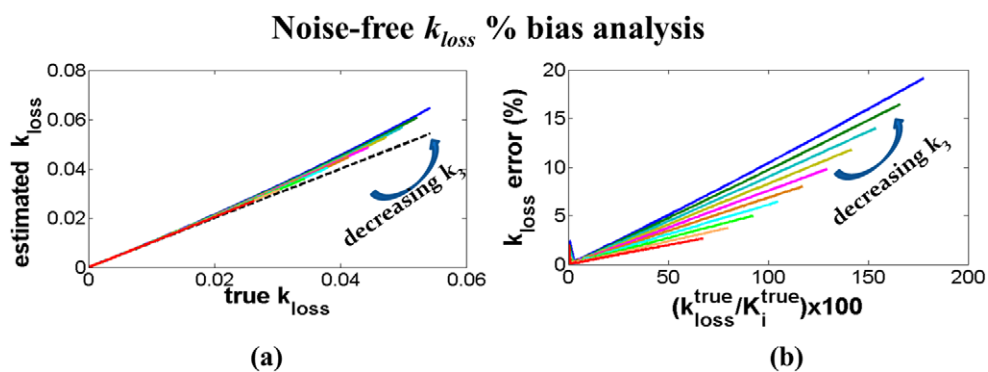


Figure 7. (a) Correlation between estimated (noise-free) and true k_{loss} and (b) plot of k_{loss} estimation error (% bias) as a function of true k_{loss}/K_i for 30–90 m acquisition protocol. The different color curves in both (a) and (b) correspond to a range of k_3 published values such that true $0 < k_{loss}/K_i < 2$. Also K_1 and k_2 are constant and correspond to the lung tumor case (table 1).

the hPatlak method, 4 different WR thresholds were evaluated starting from 0.8 up to 0.95 with a step of 0.5. In this simulation study, we considered the cardiac bed sufficient as it includes in its FOV both the left-ventricle blood pool region, from which the input function is extracted, as well as all major tissue regions referred in table 1. Besides, all particularities of WB dynamic acquisitions were retained in our simulation study, as the data were acquired at exactly the times corresponding to our multi-bed dynamic PET acquisition protocol (figure 3).

By visual inspection of K_i images in figure 8, the simulated tumor regions B1 and B2 with non-negligible underlying k_{loss} , are becoming less visible as we move from left (gPatlak) to right (sPatlak) through the intermediate (hPatlak) images. Meanwhile, visual detectability of tumors A1 and A2 is not significantly affected, since true k_{loss} is very small in their case. Moreover, the spatial image noise in the background regions is also gradually decreased along the same direction.

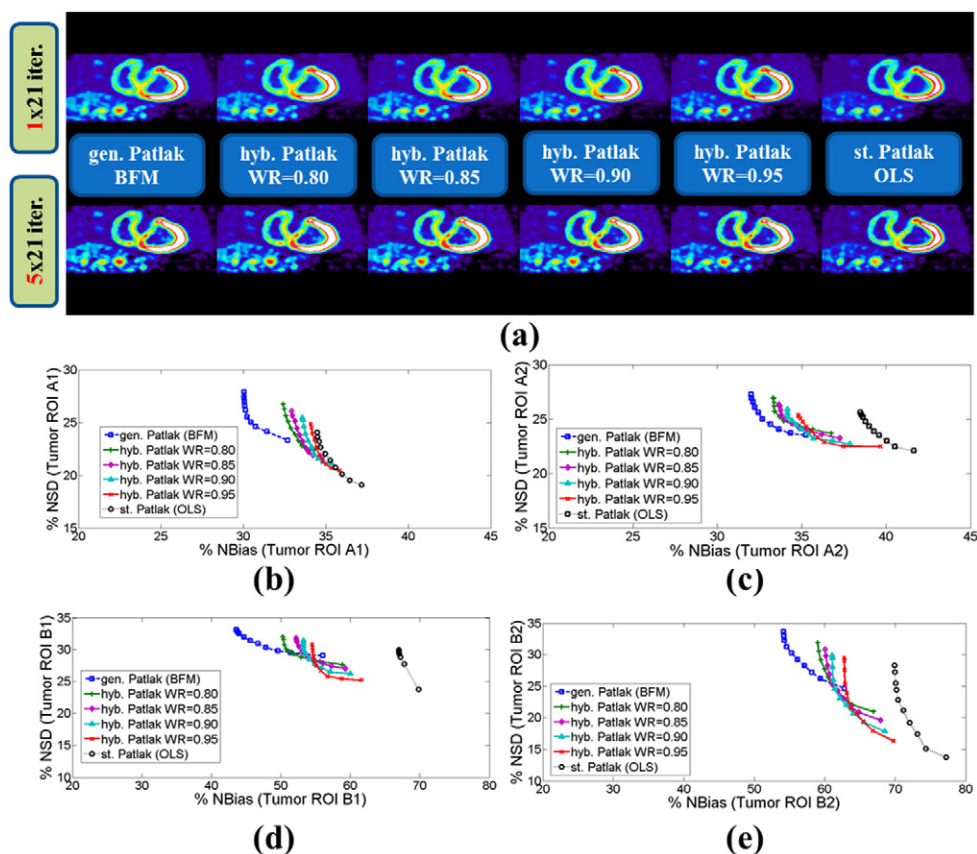


Figure 8. Simulation results: (a) parametric K_i images as generated by gPatlak (1st column), hPatlak of increasing WR thresholds (2nd–5th column) and sPatlak (6th column) methods. Indirect Patlak imaging has been conducted on reconstructed dynamic PET images after 21 (1st row) and 105 (2nd row) MLEM iterations. Normalized standard deviation (NSD) versus normalized bias (NBias) quantitative analysis for 15 noise realizations and all 6 Patlak methods above on tumor ROIs: (b) A1, (c) A2, (d) B1 and (e) B2.

The above qualitative evaluations are also confirmed from the subsequent noise versus bias quantitative analysis. The % bias is gradually increasing with WR thresholds from gPatlak to sPatlak. The most apparent bias enhancement is observed in the case of highly $k_{i\text{loss}}$ -reversible B1 and B2 tumors with a total increase of 20–40% from sPatlak to gPatlak, while the corresponding bias enhancement was only 16–18% in the case of A1 and A2 less $k_{i\text{loss}}$ -reversible tumors. Furthermore, the stronger PVE in smaller A2 and B2 regions results in relatively larger K_i underestimation and thus % K_i bias enhancement relative to A1 and B1 larger tumor regions. Finally the % noise, as evaluated across the 15 realizations, decreased gradually for hPatlak for higher WR threshold levels, with the total reduction being 10% from gPatlak to sPatlak.

In addition, in terms of TBR (figure 9) and CNR (figure 10) detectability metrics, hPatlak with a WR threshold of 0.95 consistently achieved the best scores, along all MLEM iteration steps evaluated. However, between gPatlak and sPatlak methods, the former method produced higher scores for tumors B1 and B2 while the latter performed better for tumors A1 and A2.

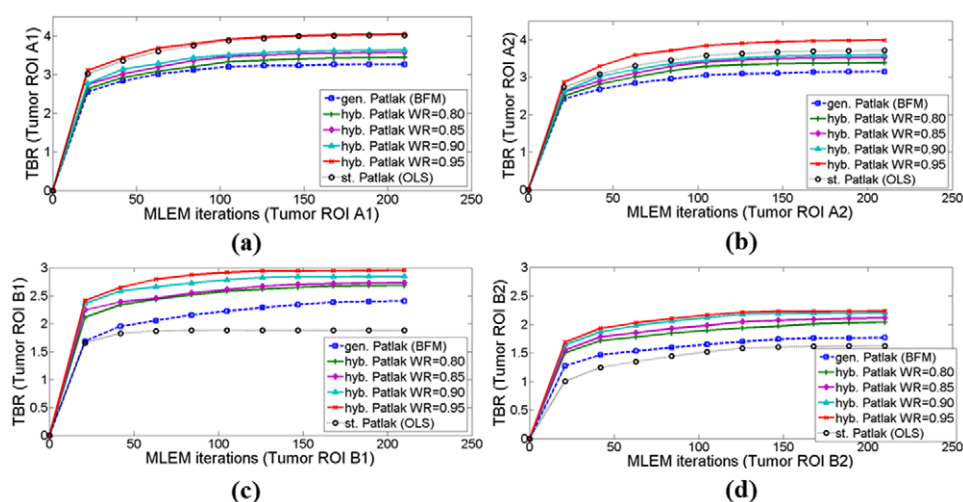


Figure 9. Simulation results: target-to-background ratio (TBR) as a function of MLEM iterations between sPatlak, gPatlak and hPatlak (various WR thresholds) K_i images for tumor ROIs: (a) A1, (b) A2, (c) B1 and (d) B2.

3.3. Clinical studies

The quantitative performance of the proposed Patlak imaging methods has also been demonstrated on $n = 11$ WB dynamic patient datasets. From these collection, a total of 6 characteristic high uptake (foci) target and respective background ROIs were selected for quantitative analysis, of which the first 4 were extracted from GE RX cases (figures 11–13) while the last two from state-of-the-art Siemens Biograph mCT scans (figure 14) in order to evaluate performance for a range of clinical study set-ups. Except for the mCT patient case, where 2 ROIs were identified (foci 1 and 2 in the thorax, figure 14), for the GE RX cases 1 characteristic ROI has been evaluated for each patient.

Figures 11–14 illustrate, for four patient cases, the reconstructed dynamic PET frames along with the SUV image, as well as the corresponding K_i images of six Patlak methods (gPatlak, hPatlak of 4 different WR thresholds and sPatlak) and the WR image. Moreover, the K_i ROI mean values between all Patlak methods as well as the TBR and CNR scores between the Patlak and SUV images are also presented.

Overall the clinical data analysis agreed with our simulation findings regarding the TBR and CNR performance of the proposed methods. Thus, hPatlak with a 0.95 WR threshold was associated with the best TBR and CNR performance among all other methods, except from GE RX patient case #5 (figure 13(c)) where gPatlak achieved the best scores, possibly because of potentially high k_{loss} presence at the particular patient ROI. Furthermore, SUV consistently provided lower TBR and CNR scores, except from mCT patient case #1, where it outperformed gPatlak CNR score, due to gPatlak higher noise levels.

In addition, gPatlak always provided the highest K_i mean value among the presented Patlak methods, suggesting reduced bias after accounting for underlying k_{loss} reversibility. However, since the ground truth is not known in clinical cases, a relatively higher K_i mean value may not be necessarily associated with less bias. For instance, K_i may be overestimated too in some cases, due to underlying kinetic heterogeneity within each voxel, as discussed later. Overall, any potential K_i overestimation effects are expected to be at least partially counteracted by PVE-induced K_i underestimation.

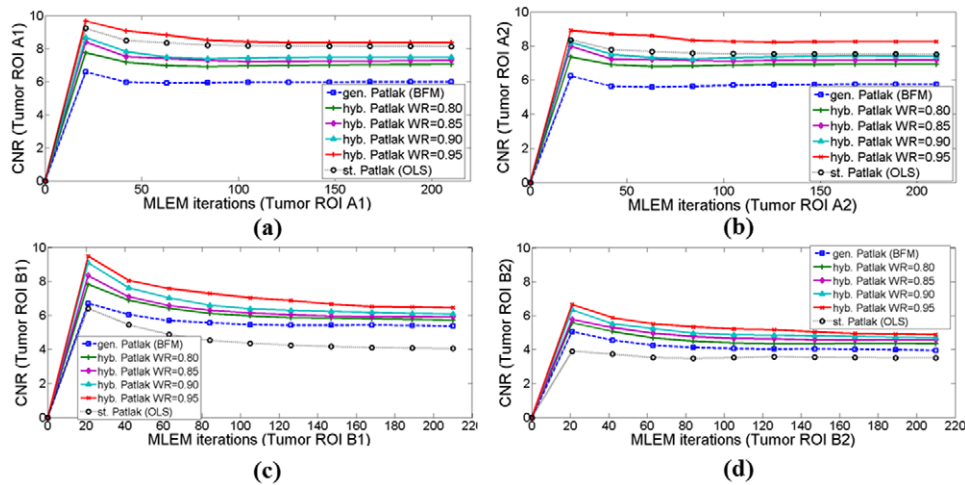


Figure 10. Simulation results: contrast-to-noise ratio (CNR) as a function of MLEM iterations between sPatlak, gPatlak and hPatlak (various WR thresholds) K_i images for tumor ROIs: (a) A1, (b) A2, (c) B1 and (d) B2.

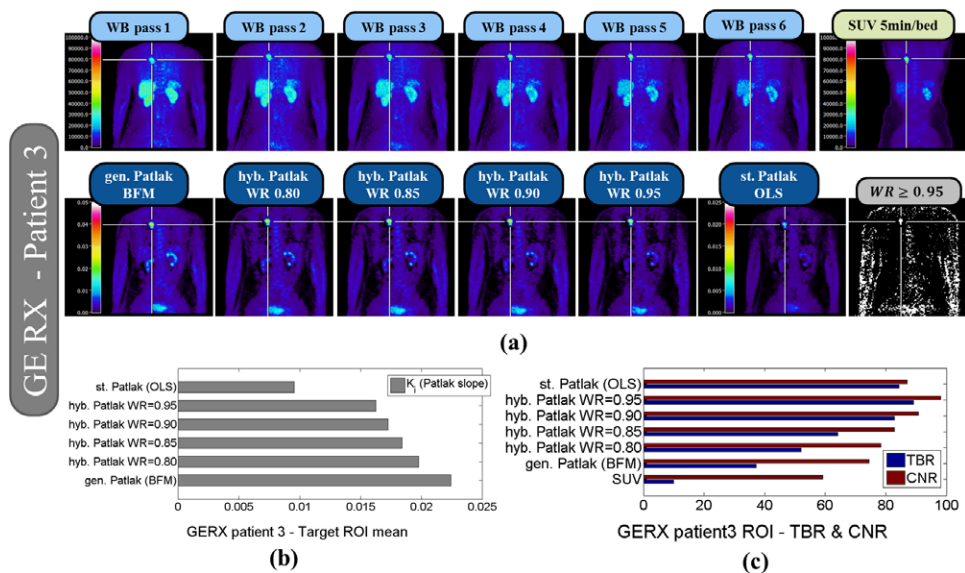


Figure 11. Clinical results: RX patient case #3, scanned on the GE Discovery RX, designated focal uptake ROI in the lung (a) 1st row: 6 WB dynamic PET passes (45 s/bed) timely-ordered from left to right and a WB static SUV PET image (5 min/bed) beginning 60 min post FDG injection, all reconstructed after 2 full OSEM iterations with 21 subsets, 2nd row (left-to-right): WB K_i images derived with gPatlak, hPatlak of increasing WR thresholds and sPatlak methods, as well as a Patlak correlation-coefficient image thresholded at WR = 0.95 (white color assigned only to voxels with values ≥ 0.95). Quantitative evaluation on the designated ROI of: (b) K_i ROI mean value and (c) TBR and CNR over all 6 Patlak methods and the SUV image.

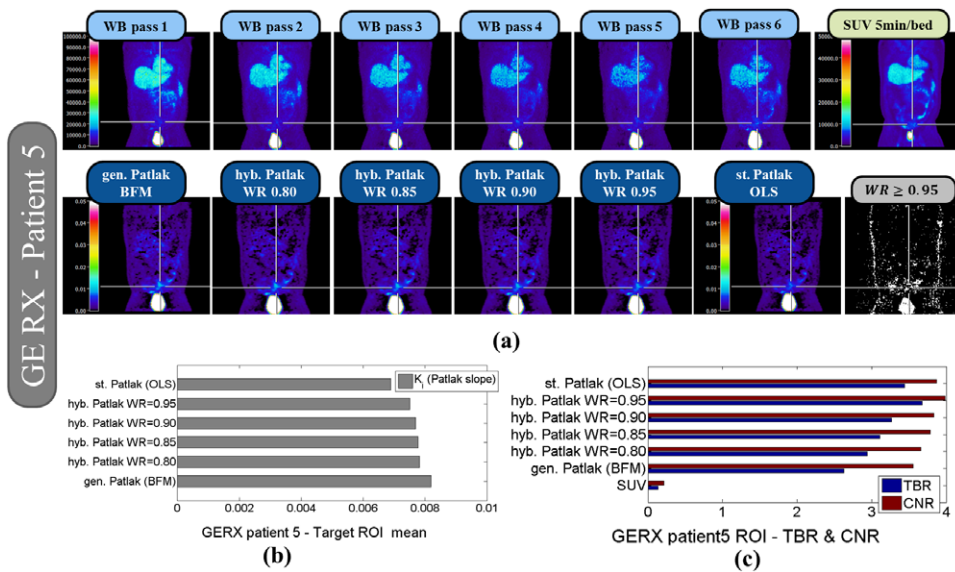


Figure 12. Clinical results: RX patient case #5, scanned on the GE Discovery RX, designated focal uptake ROI in the bowel (a), (b) and (c) same as figure 11.

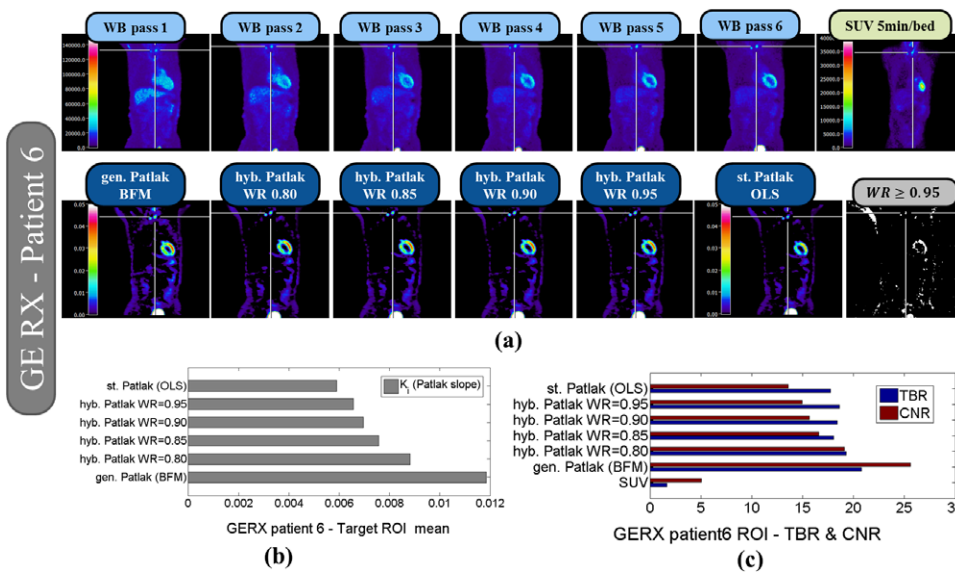


Figure 13. Clinical results: RX patient case #6, scanned on the GE Discovery RX, designated focal uptake ROI in the thyroid (a), (b) and (c) same as figure 11.

4. Discussion

4.1. Patlak graphical analysis as the method of choice for WB parametric PET imaging

The proposed gPatlak method retains, unlike full kinetic modeling, much of sPatlak robustness to high levels of noise (Graham *et al* 2000, Hoekstra *et al* 2002, Krak *et al* 2003, Tomasi

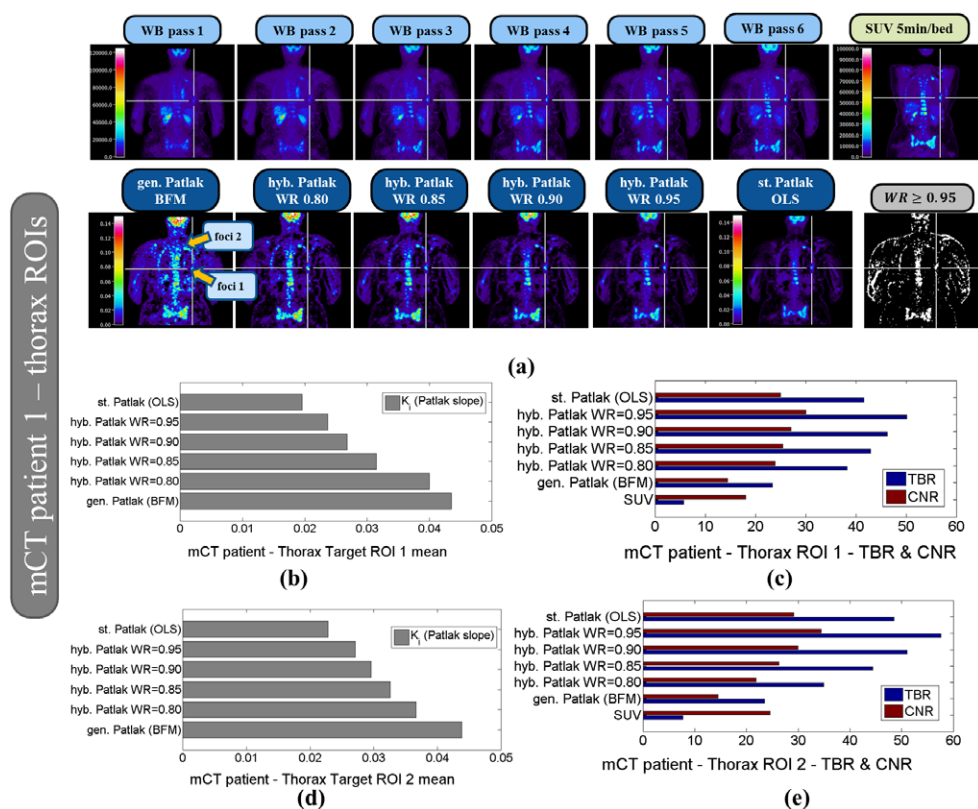


Figure 14. Clinical results: mCT patient case #1, scanned on the Siemens Biograph mCT, two designated focal uptake ROIs in the thorax (a) same as figure 11, (b) same as figure 11 but for two target ROIs: ROI 1 and (c) ROI 2.

et al 2012). Furthermore, in terms of quantitative accuracy performance, despite the gPatlak assumption for a small efflux (k_{loss}) relative to influx (K_i) rate constant (Patlak and Blasberg 1985), our results demonstrated that the relative noise-free gPatlak K_i bias is limited to less than 10% in all cases for a wide set of true k_{loss} values, ranging from zero up to extremely rare and high values (figure 6). In addition, its WB dynamic PET application remains clinically feasible because, unlike Logan graphical analysis method (Logan *et al* 1990), it only requires the time integral of the input function from time of injection and not that of every voxel TAC across the entire WB FOV. By contrast, Logan analysis additionally requires TACs for all voxels across the entire WB FOV from injection time, which can depict very rapid dynamics at early times. Application of Logan analysis is thus significantly more challenging in WB dynamic PET studies, because of the need to perform considerably faster passes which may result in significantly higher noise levels for the given sensitivity of clinical PET scanners. For instance, 10 s or less per frame at the beginning of conventional single-bed dynamic scans must now be allocated to 6 or more beds in WB mode, thus substantially limiting the scan time per bed). Moreover, the observed underestimation of the total tissue distribution volume (DV) after applying simple linear regression with Logan technique needs to be evaluated against alternative graphical analysis methods (Zhou *et al* 2009).

In addition, Patlak was also preferred in this study as it directly estimates K_i , k_{loss} and V estimates, a set of macro-parameters highly relevant with the metabolic state of normal and

tumor tissues and therefore widely applicable for our target oncology application of dynamic whole-body FDG imaging (Castell and Cook 2008). At the same time, we acknowledge the importance of other physiologically relevant macro-parameters, such as the total tissue distribution volume quantifying the capacity of a tracer binding to tissue and directly estimated by Logan method. Thus, we currently examine the future prospect of frameworks supporting additional WB graphical and multi-graphical analysis (Zhou *et al* 2009, 2010).

On the contrary, full kinetic modeling may offer a potentially more detailed, though less robust, description to the above set of macro-parameters through the non-linear estimation of individual kinetic micro-parameters (K_1 , k_2 , k_3 and k_4) with minimum assumptions for the underlying 2-tissue compartment model (Zaidi *et al* 2006). Thus, K_i could also be indirectly provided by these estimates but with significantly less robustness (Castell and Cook 2008). Finally, WB full kinetic modeling would have required finer temporal sampling for all voxel TACs across all beds from time of injection resulting in very high noise levels with current clinical PET scanner technology. Thus, the feasibility and future prospects of the less robust compartment model-based WB parametric PET imaging need to be studied separately.

4.2. Likelihood of tracer uptake reversibility between target and background regions

It has been reported that FDG k_{loss} effects are more likely observed in normal tissues (background), mainly in the liver and kidney, and less often in suspected tumor or high uptake (target) regions (Messa *et al* 1992, Hawkins *et al* 1992b, Okazumi *et al* 1992, Graham *et al* 2000, Huang *et al* 2000, Zhuang *et al* 2001, Lin *et al* 2005, Qiao *et al* 2007). This finding may, at first thought, render sPatlak more desirable over gPatlak, because a potential K_i underestimation only in the background and not the target regions, as expected in such a scenario, would actually further enhance TBR contrast and even potentially favor target CNR and detectability (Messa *et al* 1992, Okazumi *et al* 1992, Lin *et al* 2005). Therefore depending on the kinetic properties of the targeted ROI and its background, sPatlak may be preferred over gPatlak, e.g. when targeting regions with *a priori* negligible k_{loss} expectations or when the imaging task promotes detectability over quantification.

On the other hand, such potential TBR contrast enhancement may not be quantitative for tumor assessment in oncology, as it is triggered by the incidental underestimation of K_i only in background normal tissues and not the respective target regions. In addition, the probability of k_{loss} effect not being expressed in tumors versus in background can vary among different regions or different tumor types of the same region (Lin *et al* 2005). In fact, it has been shown that the probability for non-negligible k_{loss} in targeted tumor regions cannot be excluded, as in the case of hepatocellular carcinoma (HCC) tumor types (Okazumi *et al* 1992, Lin *et al* 2005).

4.3. Tumor FDG dephosphorylation and kinetics heterogeneity

As discussed in sections 1 and 4.2, FDG dephosphorylation has been suggested by numerous PET studies mainly in normal healthy tissues, such as the liver, and less often, in tumor regions, such as the case of HCC liver tumors. By contrast, a limited number of dynamic brain PET studies have reported or referred to simulation results that point to considerable overestimation (up to 20%) of regional K_i from kinetically heterogeneous regions, e.g. mixing of white and grey matter values in the same ROI, due to limited PET resolution and PVE (Schmidt *et al* 1991, 1992, Lucignani *et al* 1993, Vriens *et al* 2011).

That bias was observed when a 2-tissue compartment 4-parameter (4 K) kinetic model was applied, assuming a non-zero FDG dephosphorylation rate constant (k_4). However, the

reported bias was reduced when a 2-tissue 3-parameter (3 K) kinetic model was utilized instead, i.e. assuming zero k_4 . Schmidt *et al* (1991, 1992) attributed this effect to the tendency of the 4 K model to compensate for the reduced true FDG phosphorylation (k_3) rate constant, caused by the mixture of heterogeneous kinetics in the same region, with k_4 overestimation, thus resulting in subsequent overestimation of k_3 , K_i and k_{loss} parameters too. In the case of the 3 K model, this would not have been possible, as k_4 is forced to be zero. Thus, they concluded that the application of certain compartmental kinetic models, designed for physiologically homogeneous regions, on dynamic PET measurements extracted from heterogeneous regions may lead to erroneously overestimated K_i and k_{loss} regional estimates. Moreover, they conjectured that region-based kinetic analysis of dynamic brain FDG PET measurements cannot provide solid evidence of presence of true underlying FDG dephosphorylation, as non-zero k_4 estimates in specific regions may simply be the result of heterogeneity rather than actual dephosphorylation.

Although in this study we have only simulated physiologically homogeneous regions, there still remains the possibility for limited kinetic heterogeneity at the boundaries of the evaluated regions, especially in small tumors, due to PVE effects. In addition, the clinical data may also include suspected tumor regions with some heterogeneity. However, in all cases, our voxel-wise parametric estimation is expected to drastically limit this effect. When the input dynamic PET measurements are heterogeneous, the parameter estimation process may introduce bias in an attempt to explain heterogeneous input data, which are not expected by the model. An example of this effect could be the overestimation of k_4 , as an attempt of the 4 K model to explain a heterogeneity-induced decrease of k_3 (Schmidt *et al* 1992). In this study, we employed voxel-wise parametric estimation to minimize inter-voxel kinetic cross-contaminations, and constrain any bias propagation between K_i and k_{loss} . Nevertheless, there still remains a yet small but non-negligible probability for intra-voxel tissue kinetics heterogeneity, i.e. for each voxel TAC to be a weighted average, or mixture, of different kinetics in highly heterogeneous regions or at regional boundaries. However, our simulation results suggest that K_i bias was consistently reduced in all regions, regardless of true underlying k_{loss} effect, when gPatlak was applied. Thus, it is suggested that the positive effect in quantitative accuracy (bias) when accounting for non-zero k_{loss} , outperforms any potential negative effect of PVE-induced intra-voxel kinetic heterogeneities.

In addition, the findings of previous studies by Schmidt *et al* (1991, 1992) regarding heterogeneity-induced artificially non-zero k_{loss} estimates, though valid and quite probable, do not necessarily exclude the probability for true underlying k_{loss} effects as well, as many other studies have suggested (Messa *et al* 1992, Hawkins *et al* 1992b, Okazumi *et al* 1992, Graham *et al* 2000, Huang *et al* 2000, Zhuang *et al* 2001, Lin *et al* 2005). Moreover, we did not observe K_i bias enhancement for any of the evaluated regions when k_{loss} was assumed non-zero. In clinical results, K_i estimates were systematically higher with gPatlak, an observation consistent with both theories. However, since the ground truth is not known in clinical data, it is not possible to conjecture if gPatlak relatively higher K_i estimates suggest (i) bias enhancement, i.e. K_i overestimation due to heterogeneity effects, or (ii) bias reduction, due to properly accounting for non-zero k_{loss} , or actually (iii) a combination of both effects.

Finally, as the previous studies have also reported, the utilization of the Patlak framework to robustly estimate K_i and k_{loss} macro-parameters, as opposed to application of fully compartmental kinetic analysis (3 K or 4 K models) for the individual estimation of k_3 and k_4 micro-parameters, may have also further reduced any potential negative tissue kinetics heterogeneity effects, as Patlak methods are considered less sensitive to kinetically heterogeneous data (Mori *et al* 1990, Schmidt *et al* 1992, Lucignani *et al* 1993).

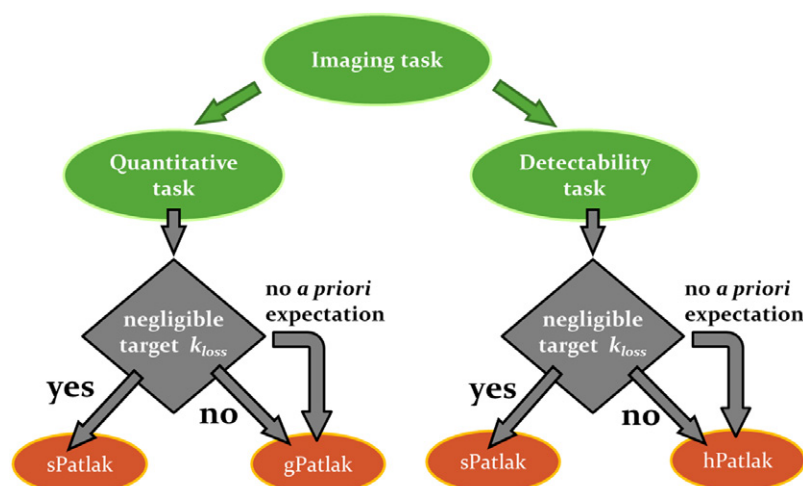


Figure 15. Flowchart illustrating our recommendations regarding the choice of WB Patlak imaging method (orange blocks) based on the imaging task (green blocks) and the *a priori* k_{loss} expectations for the target ROIs (grey blocks). According to our simulation and clinical findings, unless negligible target k_{loss} is expected, in which case sPatlak is most appropriated, either gPatlak or hPatlak is recommended depending on the imaging task performed.

4.4. Task-based recommendations for different WB Patlak methods

Having demonstrated the pros and cons of each method, in this section we provide our recommendations regarding the choice of the most appropriate Patlak method for the imaging task and underlying type of kinetics (e.g. different tracers and targets) expected in a clinical study (figure 15).

When the imaging task involves quantitative assessments and comparisons between different scans, such as in longitudinal studies or treatment response monitoring and follow-up tasks, the gPatlak method is recommended for enhanced quantification, unless there exist sufficient indications that the targeted regions exhibit negligible k_{loss} , in which case sPatlak is sufficient for robust parametric imaging. On the other hand, for imaging task prioritizing detectability hPatlak method is recommended, when no underlying kinetic information is known *a priori*, as it can potentially trigger higher TBR and CNR scores, provided the appropriate WR correlation threshold being selected. However, for target regions with expected negligible k_{loss} , we suggest the more robust sPatlak analysis for detectability tasks as well.

4.5. Generalized Patlak as a complementary framework to SUV and standard Patlak

Despite its quantitative limitations, WB static SUV imaging remains the most established PET imaging technique in the clinic. Thanks to its simplicity and routine clinical implementation, SUV imaging has allowed for the standardization of diagnostic and treatment response criteria in the clinic (Wahl *et al* 2009, Boellaard *et al* 2010). On the other hand, WB Patlak imaging methods, although potentially more accurate than SUV, are associated with higher complexity and noise levels. Yet, they are nowadays steadily gaining more attention, as emerging commercial PET technologies, such as continuous bed motion, time-of-flight and resolution modeling, help to overcome these challenges, paving the way towards their clinical adoption (Karakatsanis *et al* 2014b). Moreover, following sPatlak, the proposed gPatlak framework

can be easily applied as an additional kinetic analysis method, utilizing the same set of reconstructed images at a small computational cost.

Our primary aim here is the design of a clinically feasible multi-bed parametric PET imaging framework to enhance quantitative information content with respect to single-pass SUV imaging alone. At the same time, we recognize the important clinical value of the SUV metric as well, particularly in relation to the currently established SUV-based treatment response criteria. In this context, SUV and parametric PET imaging frameworks could efficiently complement each other. Currently, we are investigating clinically adoptable novel PET scan protocols that *simultaneously* enable WB SUV and Patlak imaging from a single acquisition performed over the conventional 60 min post-injection SUV time window (Karakatsanis *et al* 2015). This study aims to introduce additional WB Patlak imaging frameworks to enhance quantification or detectability with respect to more conventional Patlak schemes. In future work, a comparative clinical study between WB Patlak and SUV imaging method would be important so as to also assess the clinical potential of combined SUV/Patlak WB imaging.

4.6. Hybrid WB Patlak regression: pearls and pitfalls

The performance of hPatlak in enhancing suspected tumor ROI CNR and, thus, detectability, depends on the user-defined WR threshold level. A very large threshold, i.e. a value very close to unity, may substantially reduce background noise, but it may also exclude some tumor voxels from being accurately estimated with the gPatlak method, especially those situated at tumor boundaries, susceptible to PVE or at kinetically heterogeneous tumor sections. As a result, a high WR threshold is expected to reduce noise at the cost of quantification and contrast, with respect to pure gPatlak, while a low WR threshold may enhance quantification and contrast at the cost of additional noise, compared to sPatlak.

As hPatlak is targeting the enhancement of tumor detectability, a potential criterion for the choice of an appropriate WR threshold could have been the tumor CNR score either at a particular target tumor ROI or weighted averaged over a set of target ROIs, with the weights defined as the relative size, in number of voxels, of each ROI. On the other hand, CNR can be substantially different among patients or even between target ROIs of the same patient and, as such, we cannot recommend a data-independent globally optimal WR threshold. Alternatively, a data-driven algorithm could automatically select for every patient a WR threshold and respective K_i clinical image based on the highest evaluated CNR score for the target ROI or set of ROIs. In fact, other nuclear imaging studies have in the past followed similar CNR-based data-driven optimization schemes when designing reconstruction algorithms (Qi and Leahy 1999), imaging systems and scan protocols (Asma and Manjeshwar 2010, da Rocha Vaz Pato *et al* 2012).

However, since CNR scores may depend on the tumor and background ROI delineation techniques, CNR-based optimization should be exercised with care. Therefore, in this study we suggest not to necessarily optimize WR threshold based on CNR and, instead, to provide the users in the future with the flexibility to alter this parameter (analogously to sliding the color bar) for an enhanced perspective onto the suspected tumor of interest.

4.7. Future prospects

The present work has scope for significantly enhanced performance. Kinetic parameter estimation commonly involves two main steps: (i) image reconstruction of individual dynamic frames, followed by (ii) application of kinetic modeling to the resulting dynamic images.

This common process poses limitations due to the poor characterization of the complex noise distribution in the reconstructed images. On the contrary, direct 4D reconstruction schemes enable kinetic modeling within a comprehensive reconstruction framework, allowing accurate noise characterization directly in the projection-space (Tsoumpas *et al* 2008, Rahmim *et al* 2009, 2012, Tang *et al* 2010, Wang and Qi 2010, 2012, 2013). As such, 4D parametric reconstruction methods could be particularly important for gPatlak, where noise is relatively higher than sPatlak. By integrating the gPatlak model within 4D ML-EM reconstruction we expect Patlak images of both superior precision (low noise) and less noise-induced bias.

Previously, we confirmed the benefit of direct 4D reconstruction in limiting noise propagation in WB sPatlak imaging (Karakatsanis *et al* 2013b). However the convergence of the iterative algorithm can be very slow, due to the correlation between K_i and V estimates (Wang *et al* 2010). In addition, the non-linearity of gPatlak 4D reconstruction, which we are presently exploring, can further impact the convergence rates (Wang and Qi 2012, 2013). Therefore, we are investigating the utilization of optimization transfer methods to enable accelerated gPatlak 4D reconstruction (Karakatsanis *et al* 2014a).

5. Conclusion

In this work, we implemented and quantitatively assessed a family of WB parametric imaging methods, utilizing both simulated and clinical PET studies, as acquired with a clinically feasible multi-bed dynamic PET scan protocol. Specifically, we extended our standard WB Patlak (sPatlak) graphical analysis method to sufficiently account for potential underlying tracer uptake reversibility. By properly incorporating the net efflux rate constant parameter of k_{loss} in a generalized Patlak (gPatlak) imaging framework, it became possible to generate parametric WB tracer influx rate constant K_i images of enhanced quantitative accuracy, compared to SUV, including in regions with non-negligible k_{loss} , where sPatlak introduced bias. At the same time, our results also indicated reduced gPatlak robustness to high noise levels and, thus relatively lower tumor CNR scores than sPatlak, except if k_{loss} effect is strong enough to provide sufficiently high contrast to counteract any CNR losses due to background noise amplification.

Furthermore, in order to efficiently enhance tumor CNR and detectability and, at the same time, to retain sufficient quantitative accuracy, we proposed a hybrid Patlak (hPatlak) method to selectively apply gPatlak analysis only to voxel TACs exhibiting high Patlak correlation coefficients and sPatlak method elsewhere. According to both simulations and clinical results, hPatlak was always associated with the highest TBR and CNR scores, while its accuracy and precision performance was placed between that of gPatlak and sPatlak methods, thus demonstrating primary clinical usefulness mainly for detectability tasks. Finally, for the clinical study, the measured CNR in SUV images was consistently lower than that of sPatlak and gPatlak in most regions and that of hPatlak in all regions, demonstrating enhanced detectability performance for Patlak imaging over conventional SUV PET.

Although gPatlak and hPatlak schemes are presented here for WB dynamic PET clinical acquisitions, they are also applicable to more common dynamic PET protocols, such as single-bed dynamic cardiac or oncologic PET studies, where temporal sampling is continuous and noise levels are lower. Moreover, although the current study has focused on FDG scans, the proposed methods may also be applied to other PET tracers which are used in WB imaging and which exhibit considerable net efflux rate constants, such as ^{18}F -FLT and ^{18}F -fluoride bone parametric imaging (Kim *et al* 2008, Siddique *et al* 2014).

Acknowledgments

The authors would like to thank Dr Abdel K Tahari and John Crandall for assistance in recruiting patients. This work was supported by Siemens Molecular Imaging, the NIH grant 1S10RR023623 and the Swiss National Science Foundation under Grant SNSF 31003A-149957.

References

- Adams M, Turkington T, Wilson J and Wong T 2010 A systematic review of the factors affecting accuracy of SUV measurements *Am. J. Roentgenol.* **195** 310–20
- Anchors JM, Haggerty DF and Karnovsky ML 1977 Cerebral glucose-6-phosphatase and the movement of 2-deoxy-D-glucose across cell membranes *J. Biol. Chem.* **252** 7035–41
- Asma E and Manjeshwar R M 2010 Adaptive acquisition protocol design for local CNR maximization in flexible SPECT and PET scanners *IEEE Nuclear Sci. Symp. & Medical Imaging Conf. (NSS/MIC) 2010* pp 3032–7
- Basu S and Alavi A 2007 Partial volume correction of standardized uptake values and the dual time point in FDG-PET imaging: should these be routinely employed in assessing patients with cancer? *Eur. J. Nucl. Med. Mol. Imaging* **34** 1527–9
- Been L B, Suurmeijer A J, Cobben D C, Jager P L, Hoekstra H J and Elsinga P H 2004 [18F] FLT-PET in oncology: current status and opportunities *Eur. J. Nucl. Med. Mol. Imaging* **31** 1659–72
- Bentourkia M and Zaidi H 2006 Tracer kinetic modeling in nuclear medicine: theory and applications *Quantitative Analysis in Nuclear Medicine Imaging* (New York: Springer) pp 391–413
- Bentourkia M H and Zaidi H 2007 Tracer kinetic modeling in PET *PET Clin.* **2** 267–77
- Boellaard R 2011 Need for standardization of 18F-FDG PET/CT for treatment response assessments *J. Nucl. Med.* **52** 93s–100s
- Boellaard R *et al* 2010 FDG PET and PET/CT: EANM procedure guidelines for tumour PET imaging: version 1.0 *Eur. J. Nucl. Med. Mol. Imaging* **37** 181–200
- Carson R E 2005 Tracer kinetic modeling in PET *Positron Emission Tomography: Basic Science and Clinical Practice* (London: Springer) pp 127–59 (doi: 10.1007/1-84628-007-9_6)
- Castell F and Cook G J R 2008 Quantitative techniques in 18FDG PET scanning in oncology *Br. J. Cancer* **98** 1597–601
- Choi H, Yoon H J, Kim T S, Oh J H, Kim D Y and Kim S K 2013 Voxel-based dual-time 18F-FDG parametric imaging for rectal cancer: differentiation of residual tumor from postchemoradiotherapy changes *Nucl. Med. Commun.* **34** 1166–73
- Choi Y, Hawkins R A, Huang S C, Brunken R C, Hoh C K, Messa C, Nitzsche E U, Phelps M E and Schelbert H R 1994 Evaluation of the effect of glucose ingestion and kinetic model configurations of FDG in the normal liver *J. Nucl. Med.* **35** 818–23
- da Rocha Vaz Pato L, Vandenberghe S and Van Holen R 2012 Efficient optimization based on local shift-invariance for adaptive SPECT systems *IEEE Nucl. Sci. Symp. & Medical Imaging Conf. (NSS/MIC) 2012* pp 2501–8
- de Langen A J *et al* 2012 Repeatability of 18F-FDG uptake measurements in tumors: a metaanalysis *J. Nucl. Med.* **53** 701–8
- Delbeke D 1999 Oncological applications of FDG PET imaging *J. Nucl. Med.* **40** 1706–15
- Dimitrakopoulou-Strauss A, Georgoulas V, Eisenhut M, Herth F, Koukouraki S, Macke H, Haberkorn U and Strauss L 2006 Quantitative assessment of SSTR2 expression in patients with non-small cell lung cancer using 68 Ga-DOTATOC PET and comparison with 18 F-FDG PET *Eur. J. Nucl. Med. Mol. Imaging* **33** 823–30
- Dimitrakopoulou-Strauss A, Strauss L G and Rudi J 2003 PET-FDG as predictor of therapy response in patients with colorectal carcinoma *Q. J. Nucl. Med.* **47** 8–13
- Dimitrakopoulou-Strauss A, Strauss L G, Heichel T, Wu H, Burger C, Bernd L and Ewerbeck V 2002 The role of quantitative 18F-FDG PET studies for the differentiation of malignant and benign bone lesions *J. Nucl. Med.* **43** 510–8
- Doudet D J, Chan G L Y, Holden J E, McGeer E G, Aigner T A, Wyatt R J and Ruth T J 1998 6-[18F] fluoro-L-DOPA PET studies of the turnover of dopamine in MPTP-induced parkinsonism in monkeys *Synapse* **29** 225–32

- Durand E and Besson F 2015 How is the standard uptake value (SUV) linked to the influx constant in Sokoloff's model for 18 F-FDG? *Méd. Nucl.* **39** 11–7
- Eary J F and Mankoff D A 1998 Tumor metabolic rates in sarcoma using FDG PET *J. Nucl. Med.* **39** 250–4
- Feng D, Huang S C and Wang X 1993 Models for computer simulation studies of input functions for tracer kinetic modeling with positron emission tomography *Int. J. Biomed. Comput.* **32** 95–110
- Fischman A J and Alpert N M 1993 FDG-PET in oncology: there's more to it than looking at pictures *J. Nucl. Med.* **34** 6–11
- Freedman N M, Sundaram S K, Kurdziel K, Carrasquillo J A, Whatley M, Carson J M, Sellers D, Libutti S K, Yang J C and Bacharach, S L 2003 Comparison of SUV and Patlak slope for monitoring of cancer therapy using serial PET scans *Eur. J. Nucl. Med. Mol. Imaging* **30** 46–53
- Gallagher B M, Fowler J S, Guttererson N I, MacGregor R R, Wan C N and Wolf AP 1979 Metabolic trapping as a principle of radiopharmaceutical design: some factors responsible for the biodistribution of [18F]2-deoxy-2-fluoro-D-glucose *J. Comp. Assist. Tomog.* **3** 295
- Graham M M, Muzi M, Spence A M, O'Sullivan F, Lewellen T K, Link J M and Krohn K A 2002 The FDG lumped constant in normal human brain *J. Nucl. Med.* **43** 1157–66
- Graham M M, Peterson L M and Hayward R M 2000 Comparison of simplified quantitative analyses of FDG uptake *Nucl. Med. Biol.* **27** 647–55
- Grant F D, Fahey F H, Packard A B, Davis R T, Alavi A and Treves S T 2008 Skeletal PET with 18F-fluoride: applying new technology to an old tracer *J. Comp. Assist. Tomog.* **3** 295
- Groves A M, Win T, Haim S B and Ell P J 2007 Non-[18 F] FDG PET in clinical oncology *Lancet Oncol.* **8** 822–30
- Gunn R N, Lammertsma A A, Hume S P and Cunningham V J 1997 Parametric imaging of ligand-receptor binding in PET using a simplified reference region model *Neuroimage* **6** 279–87
- Gupta N, Gill H, Graeber G, Bishop H, Hurst J and Stephens T 1998 Dynamic positron emission tomography with F-18 fluorodeoxyglucose imaging in differentiation of benign from malignant lung/mediastinal lesions *Chest* **114** 1105–11
- Hasselbalch S G, Holm S, Pedersen H S, Svarer C, Knudsen G M, Madsen P L and Paulson O B 2001 The 18F-fluorodeoxyglucose lumped constant determined in human brain from extraction fractions of 18F-fluorodeoxyglucose and glucose *J. Cereb. Blood Flow Metab.* **21** 995–1002
- Hawkins R A, Choi Y, Huang S C, Hoh C K, Dahlbom M, Schiepers C, Satyamurthy N, Barrio J R and Phelps M E 1992a Evaluation of the skeletal kinetics of fluorine-18-fluoride ion with PET *J. Nucl. Med.* **33** 633–42
- Hawkins R A, Choi Y, Huang S C, Messa C, Hoh C K and Phelps M E 1992b Quantitating tumor glucose metabolism with FDG and PET *J. Nucl. Med.* **33** 339–44
- Hoekstra C J, Hoekstra O S, Stroobants S G, Vansteenkiste J, Nuyts J, Smit E F, Boers M, Twisk J W R and Lammertsma A A 2002 Methods to monitor response to chemotherapy in non-small cell lung cancer with 18F-FDG PET *J. Nucl. Med.* **43** 1304–9
- Hoekstra C J, Paglianiti I, Hoekstra O S, Smit E F, Postmus P E, Teule G J J and Lammertsma A A 2000 Monitoring response to therapy in cancer using [18F]-2-fluoro-2-deoxy-D-glucose and positron emission tomography: an overview of different analytical methods *Eur. J. Nucl. Med.* **27** 731–43
- Hoh C K, Vera D and Schiepers C 2011 Reducing effects of non-zero k_4 and metabolites in generating Patlak parametric images of FLT uptake *J. Nucl. Med.* **52** 2063
- Holden J E et al 1997 Graphical analysis of 8-fluoro-L-dopa trapping: effect of inhibition of catechol-O-methyltransferase *J. Nucl. Med.* **38** 1568–74
- Huang S C 2000 Anatomy of SUV *Nucl. Med. Biol.* **27** 643–6
- Huang S C, Phelps M E, Hoffman E J, Sideris K, Selin C J and Kuhl D E 1980 Noninvasive determination of local cerebral metabolic rate of glucose in man *Am. Physiol. Soc.* **238** E69–82
- Hübner K F, Buonocore E, Gould H R, Thie J, Smith G T, Stephens S and Dickey J 1996 Differentiating benign from malignant lung lesions using 'quantitative' parameters of FDG PET images *Clin. Nucl. Med.* **21** 941–9
- Hunter G J, Hamberg L M, Alpert N M, Choi N C and Fischman A J 1996 Simplified measurement of deoxyglucose utilization rate *J. Nucl. Med.* **37** 950–5
- Husarik D B, Miralbell R, Dubs M, John H, Giger O T, Gelet A, Cserevnyák T and Hany T F 2008 Evaluation of [18F]-choline PET/CT for staging and restaging of prostate cancer *Eur. J. Nucl. Med. Mol. Imaging* **35** 253–63
- Hustinx R, Smith R J, Benard F, Rosenthal D I, Machtay M, Farber L A and Alavi A 1999 Dual time point fluorine-18 fluorodeoxyglucose positron emission tomography: a potential method to

- differentiate malignancy from inflammation and normal tissue in the head and neck *Eur. J. Nucl. Med.* **26** 1345–8
- Hustinx R, Bénard F and Alavi A 2002 Whole-body FDG-PET imaging in the management of patients with cancer *Semin. Nucl. Med.* **32** 35–46
- Jagust W J, Seab J P, Huesman R H, Valk P E, Mathis C A, Reed B R, Coxson P G and Budinger T F 1991 Diminished glucose transport in Alzheimer's disease: dynamic PET studies *J. Cereb. Blood Flow Metab.* **11** 323–30
- Jakoby B W, Bercier Y, Conti M, Casey M E, Bendriem B and Townsend D W 2011 Physical and clinical performance of the mCT time-of-flight PET/CT scanner *Phys. Med. Biol.* **56** 2375–89
- Karakatsanis N A and Rahmim A 2014a Whole-body PET parametric imaging employing direct 4D nested reconstruction and a generalized non-linear Patlak model *Proc. SPIE* **9033** 90330Y0
- Karakatsanis N A, Lodge M A, Rahmim A and Zaidi H 2014b Introducing time-of-flight and resolution recovery image reconstruction to clinical whole-body PET parametric imaging *IEEE Nucl. Sci. Symp. & Medical Imaging Conf. (NSS/MIC) 2014* in press
- Karakatsanis N A, Lodge M A, Tahari A K, Zhou Y, Wahl R L and Rahmim A 2013a Dynamic whole-body PET parametric imaging: I. Concept, acquisition protocol optimization and clinical application *Phys. Med. Biol.* **58** 7391–418
- Karakatsanis N A, Lodge M A, Wahl R L and Rahmim A 2013b Direct 4D whole-body PET/CT parametric image reconstruction: concept and comparison versus indirect parametric imaging *J. Nucl. Med.* **54** 2133
- Karakatsanis N A, Lodge M A, Zhou Y, Casey M, Wahl R L, Subramaniam R M, Zaidi H and Rahmim A 2015 Novel multi-parametric SUV/Patlak FDG-PET whole-body imaging framework for routine application to clinical oncology *J. Nucl. Med.* **56** 625
- Karakatsanis N A, Lodge M A, Zhou Y, Mhlanga J, Chaudhry M A, Tahari A K, Wahl R L and Rahmim A 2011 Dynamic multi-bed FDG PET imaging: feasibility and optimization *IEEE Nucl. Sci. Symp. & Medical Imaging Conf. (NSS/MIC) 2011* pp 3863–70
- Karakatsanis N A, Lodge M A, Zhou Y, Wahl R L and Rahmim A 2013c Dynamic whole-body PET parametric imaging: II. Task-oriented statistical estimation *Phys. Med. Biol.* **58** 7419–45
- Karakatsanis N A, Zhou Y, Lodge M A, Casey M E, Wahl R L and Rahmim A 2013d Quantitative whole-body parametric PET imaging incorporating a generalized Patlak model *IEEE Nucl. Sci. Symp. & Medical Imaging Conf. (NSS/MIC) 2013* pp 3863–70
- Kelloff G J et al 2005 Progress and promise of FDG-PET imaging for cancer patient management and oncologic drug development *Clin. Can. Res.* **11** 2785–808
- Keyes J W Jr 1995 SUV: standard uptake or silly useless value? *J. Nucl. Med.* **36** 1836–9
- Kim C K, Gupta N C, Chandramouli B and Alavi A 1994 Standardized uptake values of FDG: body surface area correction is preferable to body weight correction *J. Nucl. Med.* **35** 164–7
- Kim S J, Lee J S, Im K C, Kim S Y, Park S A, Lee S J, Oh S J, Lee D S and Moon D H 2008 Kinetic modeling of 3'-deoxy-3'-18F-fluorothymidine for quantitative cell proliferation imaging in subcutaneous tumor models in mice *J. Nucl. Med.* **49** 2057–66
- Krak N C, van der Hoeven J J, Hoekstra O S, Twisk J W, van der Wall E and Lammertsma A A 2003 Measuring [18F] FDG uptake in breast cancer during chemotherapy: comparison of analytical methods *Eur. J. Nucl. Med. Mol. Imaging* **30** 674–81
- Kubota K, Itoh M, Ozaki K, Ono S, Tashiro M, Yamaguchi K, Akaizawa T, Yamadaand K and Fukuda H 2001 Advantage of delayed whole-body FDG-PET imaging for tumour detection *Eur. J. Nucl. Med.* **28** 696–703
- Kubota K et al 1985 Lung tumor imaging by positron emission tomography using C-11 L-methionine *J. Nucl. Med.* **26** 37–42
- Kumakura Y, Gjedde A, Danielsen E H, Christensen S and Cumming P 2006 Dopamine storage capacity in caudate and putamen of patients with early Parkinson's disease: correlation with asymmetry of motor symptoms *J. Cereb. Blood Flow Metab.* **26** 358–70
- Kumakura Y, Vernaleken I, Grunder G, Bartenstein P, Gjedde A and Cumming P 2005 PET studies of net blood-brain clearance of FDOPA to human brain: age-dependent decline of [18F]fluorodopamine storage capacity *J. Cereb. Blood Flow Metab.* **25** 807–19
- Lammertsma A A, Brooks D J, Frackowiak R S, Beaney R R, Herold S, Heather J D, Palmer A J and Jones T 1987 Measurement of glucose utilisation with [18F] 2-fluoro-2-deoxy-D-glucose: a comparison of different analytical methods *J. Cereb. Blood Flow Metab.* **7** 161–72
- Lin W Y, Tsai S C and Hung G U 2005 Value of delayed 18F-FDG-PET imaging in the detection of hepatocellular carcinoma *Nucl. Med. Commun.* **26** 315–21

- Lodge M A, Lucas J D, Marsden P K, Cronin B F, O'Doherty M J and Smith M A 1999 A PET study of 18FDG uptake in soft tissue masses *Eur. J. Nucl. Med.* **26** 22–30
- Logan J, Fowler J S, Volkow N D, Wolf A P, Dewey S L, Schlyer D J, MacGregor R R, Hitzemann R, Bendriem B, Gatley S J and Christman D R 1990 Graphical analysis of reversible radioligand binding from time-activity measurements applied to [N-11C-methyl]-(-)-cocaine PET studies in human subjects *J. Cereb. Blood Flow Metab.* **10** 740–7
- Lortie M, Beanlands R S, Yoshinaga K, Klein R and DaSilva J N 2007 Quantification of myocardial blood flow with 82Rb dynamic PET imaging *Eur. J. Nucl. Med. Mol. Imaging* **34** 1765–74
- Lucignani G, Schmidt K C, Moresco R M, Striano G, Combo F, Sokoloff L and Fazio F 1993 Measurement of regional cerebral glucose utilization with fluorine-18-FDG and PET in heterogeneous tissues: theoretical considerations and practical procedure *J. Nucl. Med.* **34** 360–9
- Matthies A, Hickeson M, Cuchiara A and Alavi A 2002 Dual time point 18F-FDG PET for the evaluation of pulmonary nodules *J. Nucl. Med.* **43** 871–5
- Messa C, Choi Y, Hoh C K, Jacobs E L, Glaspy J A, Rege S, Nitzsche E, Huang S C, Phelps M E and Hawkins R A 1992 Quantification of glucose utilization in liver metastases: parametric imaging of FDG uptake with PET *J. Comput. Assist. Tomogr.* **16** 684–9
- Mori K, Schmidt K, Jay T, Palombo E, Nelson T, Lucignani G, Pettigrew K, Kennedy C and Sokoloff L 1990 Optimal duration of experimental period in measurement of local cerebral glucose utilization with the deoxyglucose method. *J. Neurochem.* **54** 307–19
- Nakamoto Y, Higashi T, Sakahara H, Tamaki N, Kogire M, Hosotani R, Imamura M and Konishi J 2000 Delayed 18F-fluoro-2-deoxy-D-glucose positron emission tomography scan for differentiation between malignant and benign lesions in the pancreas *Cancer* **89** 2547–54
- Nelson C A, Wang J Q, Leav I and Crane P D 1996 The interaction among glucose transport, hexokinase, and glucose-6-phosphatase with respect to 3H-2-deoxyglucose retention in murine tumor models *Nucl. Med. Biol.* **23** 533–41
- Nishiyama Y, Yamamoto Y, Fukunaga K, Kimura N, Miki A, Sasakawa Y, Wakabayashi H, Satohand K and Ohkawa M 2006 Dual-time-point 18F-FDG PET for the evaluation of gallbladder carcinoma *J. Nucl. Med.* **47** 633–8
- Okazumi S, Dimitrakopoulou-Strauss A, Schwarzbach M and Strauss L 2009 Quantitative, dynamic 18F-FDG-PET for the evaluation of soft tissue sarcomas: relation to differential diagnosis, tumor grading and prediction of prognosis *Hel. J. Nucl. Med.* **12** 223–8
- Okazumi S, Isono K, Enomoto K, Kikuchi T, Ozaki M, Yamamoto H, Hayashi H, Asano T and Ryu M 1992 Evaluation of liver tumors using fluorine-18-fluorodeoxyglucose PET: characterization of tumor and assessment of effect of treatment *J. Nucl. Med.* **33** 333–9
- Oo J H, Karakatsanis N, Rahmim A, Lodge M and Wahl R 2013 A novel imaging method for assessing vessel wall inflammation: dynamic multi-bed PET parametric imaging *J. Nucl. Med.* **54** 1670
- Paquet N, Albert A, Foidart J and Hustinx R 2004 Within-patient variability of 18F-FDG: standardized uptake values in normal tissues *J. Nucl. Med.* **45** 784–8
- Patlak C S and Blasberg R G 1985 Graphical evaluation of blood-to-brain transfer constants from multiple-time uptake data generalizations *J. Cereb. Blood Flow Metab.* **5** 584–90
- Patlak C S, Blasberg R G and Fenstermacher J 1983 Graphical evaluation of blood-to-brain transfer constants from multiple-time uptake data *J. Cereb. Blood Flow Metab.* **3** 1–7
- Phelps M E, Huang S C, Hoffman E J, Selin C, Sokoloff L and Kuhl D E 1979 Tomographic measurement of local cerebral glucose metabolic rate in humans with (F-18) 2-fluoro-2-deoxy-D-glucose: validation of method *Ann. Neurol.* **6** 371–88
- Prytz H, Keiding S, Björnsson E, Broomé U, Almer S, Castedal M and Munk O L 2006 Dynamic FDG-PET is useful for detection of cholangiocarcinoma in patients with PSC listed for liver transplantation *Hepatology* **44** 1572–80
- Qi J and Leahy R M 1999 A theoretical study of the contrast recovery and variance of MAP reconstructions from PET data *IEEE Trans Med. Image* **18** 293–305
- Qiao H, Bai J, Chen Y and Tian J 2007 Kidney modelling for FDG excretion with PET *Int. J. Biomed. Imaging* **2007** 63234
- Rahmim A, Tang J and Zaidi H 2009 Four-dimensional (4D) image reconstruction strategies in dynamic PET: beyond conventional independent frame reconstruction *Med. Phys.* **36** 3654–70
- Rahmim A, Zhou Y, Tang J, Lu L, Sossi V and Wong D F 2012 Direct 4D parametric imaging for linearized models of reversibly binding PET tracers using generalized AB-EM reconstruction *Phys. Med. Biol.* **57** 733–55

- Sadato N, Tsuchida T, Nakaumra S, Waki A, Uematsu H, Takahashi N, Hayashi N, Yonekura Y and Ishii Y 1998 Non-invasive estimation of the net influx constant using the standardized uptake value for quantification of FDG uptake of tumours *Eur. J. Nucl. Med.* **25** 559–64
- Sanz J and Fayad Z A 2008 Imaging of atherosclerotic cardiovascular disease *Nature* **451** 953–57
- Sayre G A, Franc B L and Seo Y 2011 Patient-specific method of generating parametric maps of Patlak Ki without blood sampling or metabolite correction: a feasibility study *Int. J. Mol. Imaging* **2011** 1–12
- Schmidt K, Lucignani G, Moresco R M, Rizzo G, Gilardi M C, Messa C, Colombo F, Fazio F and Sokoloff L 1992 Errors introduced by tissue heterogeneity in estimation of local cerebral glucose utilization with current kinetic models of the [¹⁸F]-fluorodeoxyglucose method *J. Cereb. Blood Flow Metab.* **12** 823–34
- Schmidt K, Mies G and Sokoloff L 1991 Model of kinetic behavior of deoxyglucose in heterogeneous tissues in brain: a reinterpretation of the significance of parameters fitted to homogeneous tissue models *J. Cereb. Blood Flow Metab.* **11** 10–24
- Siddique M, Blake G M, Frost M L, Moore A E B, Puri T, Marsden P K and Fogelman I 2012 Estimation of regional bone metabolism from whole-body 18F-fluoride PET static images *Eur. J. Nucl. Med. Mol. Imaging* **39** 337–43
- Siddique M, Frost M L, Blake G M, Moore A E, Al-Beyatti Y, Marsden P K and Fogelman I 2011 The precision and sensitivity of 18F-fluoride PET for measuring regional bone metabolism: a comparison of quantification methods *J. Nucl. Med.* **52** 1748–55
- Siddique M, Frost M L, Moore A E B, Fogelman I and Blake G M 2014 Correcting 18F-fluoride PET static scan measurements of skeletal plasma clearance for tracer efflux from bone *Nucl. Med. Commun.* **35** 303–10
- Sossi V, Doudet D J and Holden J E 2001 A reversible tracer analysis approach to the study of effective dopamine turnover *J. Cereb. Blood Flow Metab.* **21** 469–76
- Sundaram S K, Freedman N M, Carrasquillo J A, Carson J M, Whatley M, Libutti S K, Sellers D and Bacharach S L 2004 Simplified kinetic analysis of tumor 18F-FDG uptake: a dynamic approach *J. Nucl. Med.* **45** 1328–33
- Suzuki S, Toyota T, Suzuki H and Goto Y 1984 Partial purification from human mononuclear cells and placental plasma membranes of an insulin mediator which stimulates pyruvate dehydrogenase and suppresses glucose-6-phosphatase *Arch. Biochem. Biophys.* **235** 418–26
- Tang J, Kuwabara H, Wong D F and Rahmim A 2010 Direct 4D reconstruction of parametric images incorporating anato-functional joint entropy *Phys. Med. Biol.* **55** 4261–72
- Thie J A 2004 Understanding the standardized uptake value, its methods, and implications for usage *J. Nucl. Med.* **45** 1431–4
- Thielemans K, Tsoumpas C, Mustafovic S, Beisel T, Aguiar P, Dikaos N and Jacobson M W 2012 STIR: software for tomographic image reconstruction release 2 *Phys. Med. Biol.* **57** 867–83
- Thorwarth D, Eschmann S M, Paulsen F and Alber M 2005 A kinetic model for dynamic [¹⁸F]-Fmiso PET data to analyse tumour hypoxia *Phys. Med. Biol.* **50** 2209–24
- Tomasi G, Turkheimer F and Aboagye E 2012 Importance of quantification for the analysis of PET data in oncology: review of current methods and trends for the future *Mol. Image Biol.* **14** 131–46
- Torizuka T, Nobezawa S, Momiki S, Kasamatsu N, Kanno T, Yoshikawa E, Futatsubashi M, Okada H and Ouchi Y 2000 Short dynamic FDG-PET imaging protocol for patients with lung cancer *Eur. J. Nucl. Med.* **27** 1538–42
- Torizuka T et al 1995 *In vivo* assessment of glucose metabolism in hepatocellular carcinoma with FDG-PET *J. Nucl. Med.* **36** 1811–7
- Tsoumpas C, Turkheimer F E and Thielemans K 2008 A survey of approaches for direct parametric image reconstruction in emission tomography *Med. Phys.* **35** 3963–71
- Vriens D, Disselhorst J A, Oyen W J G, de Geus-Oei L F and Visser E 2011 Quantitative assessment of heterogeneity in tumor metabolism using FDG-PET *Int. J. Radiat. Oncol. Biol. Phys.* **82** e725–31
- Wahl R L and Buchanan J 2002 *Principles and Practice of Positron Emission Tomography* (Philadelphia, PA: Williams & Wilkins) pp 1–462
- Wahl R L, Jacene H, Kasamon Y and Lodge M A 2009 From RECIST to PERCIST: evolving considerations for PET response criteria in solid tumors *J. Nucl. Med.* **50** 122S–50S
- Wang G and Qi J 2010 Acceleration of the direct reconstruction of linear parametric images using nested algorithms *Phys. Med. Biol.* **55** 1505–17
- Wang G and Qi J 2012 An optimization transfer algorithm for nonlinear parametric image reconstruction from dynamic PET data *IEEE Trans. Med. Imaging* **31** 1977–88

- Wang G and Qi J 2013 Direct estimation of kinetic parametric images for dynamic PET *Theranostics* **3** 802–15
- Wu H M, Bergsneider M, Glenn T C, Yeh E, Hovda D A, Phelps M E and Huang S C 2003 Measurement of the global lumped constant for 2-deoxy-2-[18 F] fluoro-D-glucose in normal human brain using [15 O] water and 2-deoxy-2-[18 F] fluoro-D-glucose positron emission tomography imaging: a method with validation based on multiple methodologies *Mol. Imag. Biol.* **5** 32–41
- Zasadny K R and Wahl R L 1993 Standardized uptake values of normal tissues at PET with 2-[fluorine-18]-fluoro-2-deoxy-D-glucose: variations with body weight and a method for correction *Radiology* **189** 847–850
- Zasadny K R and Wahl R L 1996 Enhanced FDG-PET tumor imaging with correlation-coefficient filtered influx-constant images *J. Nucl. Med.* **37** 371–4
- Zhou Y, Ye W, Brašić J R and Wong D F 2010 Multi-graphical analysis of dynamic PET *Neuroimage* **49** 2947–57
- Zhou Y, Ye W, Brašić J R, Crabb A H, Hilton J and Wong D F 2009 A consistent and efficient graphical analysis method to improve the quantification of reversible tracer binding in radioligand receptor dynamic PET studies *Neuroimage* **44** 661–70
- Zhuang H, Pourdehnad M, Lambright E S, Yamamoto A J, Lanuti M, Li P, Mozley P D, Rossman M D, Albelda S M and Alavi A 2001 Dual time point 18F-FDG PET imaging for differentiating malignant from inflammatory processes *J. Nucl. Med.* **42** 1412–7